



A general inflow turbulence generator for large eddy simulation

S.H. Huang^{a,b}, Q.S. Li^{b,*}, J.R. Wu^b

^a School of Engineering Science, University of Science and Technology of China, Hefei, China

^b Department of Building and Construction, City University of Hong Kong, Kowloon, Hong Kong

ARTICLE INFO

Article history:

Received 31 July 2007

Received in revised form

18 May 2010

Accepted 4 June 2010

Available online 22 June 2010

Keywords:

Computational wind engineering

Computational fluid dynamics

Large eddy simulation

Random flow generation

ABSTRACT

This paper presents a general inflow turbulence generator for numerical simulation of a spatially correlated turbulent flow field. The novel inflow turbulence generator is developed based on the discretizing and synthesizing random flow generation (DSRFG) technique that is proved to be able to generate a fluctuating turbulent flow field satisfying any given spectrum. Then, the techniques of aligning and remapping are incorporated in the inflow turbulence generator for generation of an inhomogeneous and anisotropic turbulent flow field following arbitrary target spectra in three orthogonal directions. The performance of the present inflow turbulence generator is compared with that of Smirnov's random flow generation (RFG) method. Detailed numerical studies show that the proposed inflow turbulence generator can strictly guarantee divergence-free condition without any additional improving step and synthetically generate inflows satisfying prescribed spatial anisotropy and correlation conditions. It is demonstrated through numerical examples that the inflow turbulence generator developed in this study is an effective tool for generation of a spatially correlated turbulent flow field for large eddy simulation (LES).

© 2010 Elsevier Ltd. All rights reserved.

1. Introduction

With development of computational fluid dynamics (CFD) techniques, large eddy simulation (LES) has been widely applied to simulate turbulent flows of engineering interest. A very important issue to ensure obtaining accurate LES results is to generate a random flow field as an inflow boundary condition (inflow turbulence) satisfying prescribed spatial correlations and turbulence characteristics. There are several techniques relevant to the title problem have been developed in the past (Kondo et al., 1997; Smirnov et al., 2001; Jarrin et al., 2006; Tamura, 2000), which can be classified into three kinds of methods: recycling methods, precursor databases and synthetic turbulence (Keating et al., 2004). The recycling methods and precursor databases are two basic approaches for inflow turbulence generation. A review of these methods can be found in Liu and Pletcher (2006). Hence, only the synthetic turbulence generation methods are discussed below, which can be grouped into the following three categories.

The first category of the methods for inflow turbulence generation was initiated by Hoshiya (1972), then developed by Iwatani (1982), Maruyama and Morikawa (1994), and recently modified by Kondo et al. (1997), in which the power spectral density and cross-spectral density obtained from FFT analysis of time series of wind velocity fluctuations are used to construct the

trigonometric series with the Gaussian random coefficients. Then, the velocity fluctuations are expressed by a series of cosine and sine functions. The coefficients of the functions are obtained by solving a system of linear equations. Such methods have an advantage that the target spectral density and root mean square (rms) value can be imposed in the generation procedure for a random flow field and thus the prescribed target characteristics can be guaranteed. However, no divergence-free condition is imposed in the generation process so that the condition of continuity may not be ensured for the generated flow field, which may affect solution convergence in LES. Therefore, the generated inflow turbulence has to be modified to satisfy the continuity equation. Kondo et al. (1997) presented a method developed by Shirani et al. (1981) to deal with the divergence-free operation, but the resulted turbulence power spectral density was deviated from the target to some extent and an extra constraint to time interval of velocity fluctuation was imposed to avoid the undesired grid skewness. Furthermore, the generation procedure was performed point by point sequentially, which is not suitable for conducting parallel computation and the generated inflow turbulence must be stored before carrying out LES. Recently, a method called biorthogonal decomposition algorithm introduced by Aubry et al. (1991) has been developed by Hemon and Santi (2007) for generation of a turbulent velocity field. The main idea of this method is to carry out a deterministic decomposition of a space-time signal by assuming-integrability only. The major advantage of this method is to generate a turbulent flow field satisfying specified spatial correlations. But, the shortcomings

* Corresponding author. Tel.: +852 27844677; fax: +852 27887612.
E-mail address: bcqli@cityu.edu.hk (Q.S. Li).

mentioned above still exist in this method, for instance, the divergence-free condition cannot be guaranteed.

The second category of the methods was developed based on a variant of spectral method for generation of an isotropic continuous flow field, which was initially proposed by Kraichnan (1970), further developed by several researchers including Li et al. (1994), Bechara et al. (1994), Fung et al. (1992), Smirnov et al. (2001), Klein et al. (2003), and Batten et al. (2004). In Smirnov's method (Smirnov et al., 2001), turbulence length scale and time scale are incorporated into the basic model proposed by Kraichnan (1970) to generate an isotropic divergence-free fluctuating velocity field with the target turbulence length and time scales, while the inhomogeneous and anisotropic turbulence characteristics can be realized by a scaling and orthogonal transformation of the resulted flow field with a given anisotropic velocity correlation tensor. The method proposed by Batten et al. (2004) is somehow similar to Smirnov's method, except that the wave numbers are elongated in the direction of larger Reynolds stresses by factors constructed with given moments and spectra, thus producing more realistic, anisotropic eddies into the flow field. Compared with Kondo's method (Kondo et al., 1997), the major advantages of the second category of the methods are: (1) the generated flow field is divergence-free in nature even after orthogonal transformation, no modification is needed; (2) the spatial anisotropy of turbulence length scale, which may be important in simulation of realistic flows, can also be satisfied. Besides, the generation procedure is independent for each point, so it is very suitable for conducting parallel computation. However, a major disadvantage of such methods is that the spectral density of the generated turbulent flow field only follows Gaussian's spectral model. As shown in Fig. 1, the Gaussian model was originally designed to approximate the energy-containing subrange of turbulence only, which means that the energy in the inertial subrange and the dissipation subrange may be neglected in the turbulent flow field generated by Smirnov's method.

According to study of Lumley and Panofsky (1964), in a high Reynolds-number flow such as wind flow in atmospheric boundary layer, the energy-containing subrange of turbulence contains the bulk of the turbulent energy and energy production source. The inertial subrange contains the energy transferred from large scales of the energy-containing range to smaller scales of the dissipation range while the dissipation range is a range where turbulence energy is converted to internal energy. Obviously, the

energy contained in the dissipation range is in the same order with the Kolmogorov scale, η ; which may be less significant for LES, since η is much smaller than the filtering length scale of LES. But, for the energy contained in the inertial subrange, as mentioned previously, the length scale lies between the integral length scale L and the Kolmogorov scale η . This may be significant for LES, since a comparative part of energy with length scale greater than the filtering length scale of LES can be resolved. In fact, the von Karman spectral model covers both the energy-containing subrange and the inertial subrange, so generation of a fluctuating velocity field satisfying the spectrum of the von Karman model or a realistic spectrum is essential to ensure accurate LES for evaluation of wind effects on buildings and structures.

It is worthy noting that in computational wind engineering (CWE) applications, generation of an inflow turbulence satisfying a target spectrum such as the von Karman model is of great significance for evaluation of wind effects on building and structures by LES, since a realistic turbulence spectrum of wind speed fluctuation in atmospheric boundary layer was found to obey the von Karman model (Lumley and Panofsky, 1964; Hinze, 1975; Li et al., 2004, 2007, 2005) and it was recognized that the turbulent eddies in the inertial subrange have a non-negligible effect on wind-induced fluctuating forces on buildings and structures.

An approach by Sergent, explained in Mathey et al. (2006), belongs to the third category of the synthetic turbulence generation methods, in which a random 2D vortex method is used at inlet to add perturbations on a specified mean velocity profile. This method can generate a velocity field that is both temporally and spatially correlated, provide reasonable profiles of mean turbulence kinetic energy and mean dissipation rate at the inlet. However, different from the methods discussed above, the target spectrum and statistical characteristics of inflow turbulence as well as inhomogeneity and anisotropy of turbulence are not explicitly expressed in its generating procedure.

The aim of this study is to establish a general inflow turbulence generator capable of generating a spatially correlated turbulent flow field satisfying the von Karman model or an arbitrary spectrum. In this paper, an efficient random flow generation technique is developed based on the second category of the synthetic turbulence generation methods, thus inheriting most advantages of such method, especially the divergence-free property. Besides, proper choices of several key parameters, such as spatial scaling factor, sampling number etc., are discussed in this paper. Both Smirnov's method and the present method are applied to numerical simulation of wind effects on a tall building. Finally, the computational results of the wind-induced forces and flow field are compared with experimental data obtained in a wind-tunnel test to verify the accuracy and effectiveness of the proposed method.

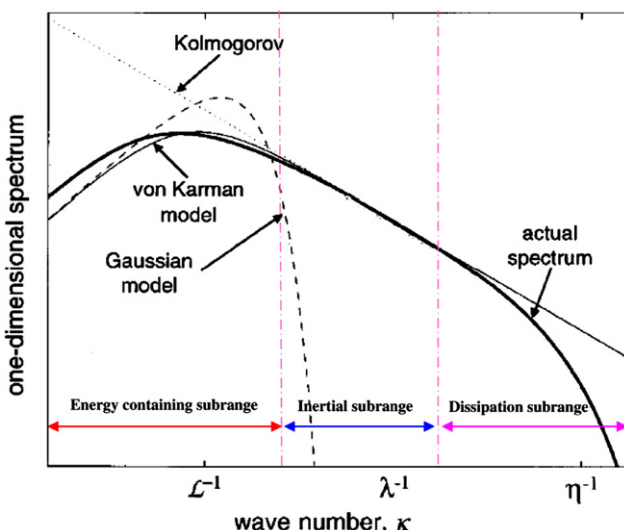


Fig. 1. Three turbulence subranges at high-Reynolds-numbers and display of spectra including the von Karman spectrum and the Gaussian spectral model.

2. Methodology

2.1. Review of Smirnov's random flow generation (RFG) technique

Before presenting the new random flow generation method developed in this paper, it is better to provide a brief introduction of the RFG method proposed by Smirnov et al. (2001). This method involves scaling and orthogonal transformation operations applied to a continuous flow field generated by a superposition of harmonic functions. The first step in construction of a fluctuating velocity field is to find an orthogonal transformation tensor a_{ij} that would diagonalize a given anisotropic velocity

correlation tensor r_{ij} .

$$a_{mi}a_{nj}r_{ij} = \delta_{mn}c_{(n)}^2 \quad (1)$$

$$a_{ik}a_{kj} = d_{ij} \quad (2)$$

Then an intermediate velocity u_i as a sum of sine and cosines with random phases and amplitudes are constructed,

$$u_i(\vec{x}, t) = \sqrt{\frac{2}{N}} \sum_{n=1}^N [p_i^n \cos(\tilde{k}_j^n \tilde{x}_j + \omega_n \tilde{t}) + q_i^n \sin(\tilde{k}_j^n \tilde{x}_j + \omega_n \tilde{t})] \quad (3)$$

$$\tilde{x}_j = \frac{x_j}{l}, \quad \tilde{t} = \frac{t}{\tau}, \quad c = \frac{l}{\tau}, \quad \tilde{k}_j^n = k_j^n \frac{c}{c_{(j)}} \quad (4)$$

$$p_i^n = \varepsilon_{ijm} \xi_j^n k_m^n, \quad q_i^n = \varepsilon_{ijm} \xi_j^n k_m^n \quad (5)$$

$$\xi_i^n, \xi_j^n, \omega_n \in N(0, 1), \quad k_i^n \in N\left(0, \frac{1}{2}\right)$$

where l, τ are the length and time-scales of turbulence, which can be calculated from the turbulence kinetic energy k and the turbulence dissipation rate ε or determined based on experimental results; ε_{ijm} is the permutation tensor used in vector product operation, and $N(M, \sigma)$ represents a normal distribution with mean of M and standard deviation of σ . k_j^n and ω_n , respectively, represent a sample of n wave-number vectors and frequencies of the modeled turbulence spectrum, which is expressed by

$$E(k) = 16(2/\pi)^{1/2} k^4 \exp(-2k^2) \quad (6)$$

Final fluctuating flow field will be obtained by applying a scaling and orthogonal transformation to the flow field u_i generated in the previous steps,

$$u'_i = c_{(i)} u_i \quad (7)$$

$$u_i^f = a_{ik} u'_k \quad (8)$$

The outcome of the procedure is to produce a time-dependent flow field $u_i^f(x_j, t)$ with correlation functions $\bar{u}_i u_j$ equal to r_{ij} , turbulence length and time scales equal to l and τ , respectively. Smirnov et al. (2001) proved that this flow field is divergence free for a homogeneous turbulent flow field and high degree divergence-free for an inhomogeneous turbulent flow field.

Fig. 2 shows a spectrum of longitudinal fluctuating wind velocity generated by the above introduced procedure for incident

wind flow with longitudinal turbulence intensity $I_u=8\%$ and turbulence integral length scale $L_u=0.3$ m. A spectrum measured by Li (1996) in wind tunnel testing for approaching wind flow with the same turbulence characteristics and the curves determined by the von Karman model and the Gaussian model are shown in Fig. 2 for comparison purposes. It is evident that the spectrum generated by Smirnov's method decays rapidly in the inertial subrange, approaching the curve of the Gaussian model. The measured spectrum is well matched by the curve of the von Karman model. As discussed previously, generation of a fluctuating wind flow field satisfying a target spectrum such as the von Karman model will make the resulted turbulent flow field more realistic for wind engineering applications.

After inspecting the generation procedure introduced above, it is found that the scaling and orthogonal transformation procedure (Eqs. (7) and (8)) is relatively independent of the generation approach (Eqs. (3)–(5)) for simulation of an isotropic fluctuating flow field, which means that this procedure may be independently applied to other methods to account for anisotropic effects. In the next section, this procedure will be used as an optional operation in the new method for generation of a random flow field satisfying given anisotropic velocity correlations.

2.2. A general inflow turbulence generation method

In this section, a new inflow turbulence generation method that can produce a fluctuating velocity field satisfying any given spectrum including the von Karman spectrum is proposed. This method is developed based on a procedure by Kraichnan (1970) for generation of an isotropic continuous flow field satisfying a spectrum of Dirac function.

2.2.1. Discretization of a continuous spectrum

According to the study of Kraichnan (1970), an isotropic fluctuating velocity field in \mathbf{x} space can be synthesized by the following superposition of harmonic functions:

$$u_i(\mathbf{x}, t) = \sum_{n=1}^N [p_i^n \cos(k_j^n x_j + \omega_n t) + q_i^n \sin(k_j^n x_j + \omega_n t)] \quad (9)$$

where $p_i^n, \xi_j^n, k_j^n, q_i^n, \xi_j^n, \omega_n$, are defined as the same as those in Eq. (5). In fact, several kinds of fluctuating velocity fields satisfying different spectra can be generated by changing the distribution of k_i^n in Eq. (9). For example, if k_i^n is isotropically distributed on the

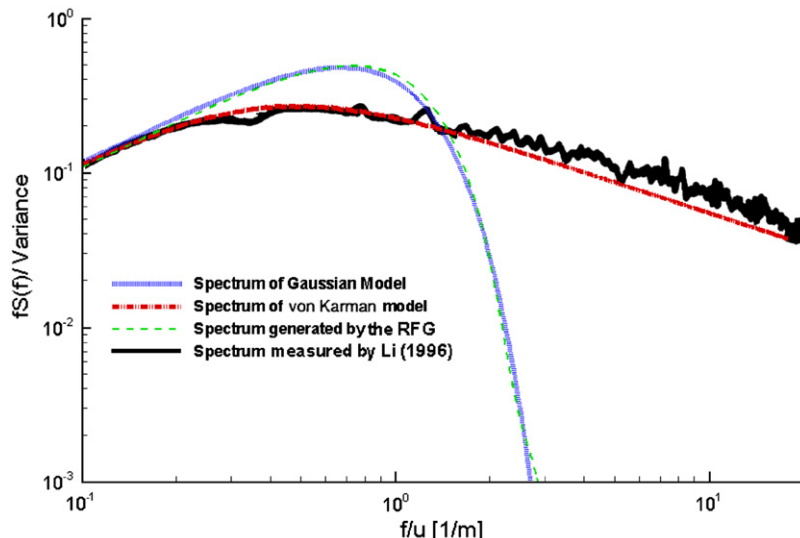


Fig. 2. Comparison of the simulated spectra with that from measurement ($I_u=8\%$, $L_u=0.3$ m).

surface of a sphere (3D), or circle (2D), of radius k_0 , the resulted velocity field satisfies the spectrum $E_1(k) = (3/2)v_0^2\delta(k-k_0)$ (3D spectrum) or $E_3(k) = v_0^2\delta(k-k_0)$ (2D spectrum), where v_0 is rms of velocity in any direction. If k_i^n is picked from a Gaussian distribution with standard deviation of $k_0/2$ or $k_0/\sqrt{3}$, the resulted velocity field satisfies the spectrum $E_2(k) = 16(2/\pi)^{1/2}v_0^2k_0^{-5}\exp(-2k^2/k_0^2)$ or $E_4(k) = 4.5k_0^{-4}\exp(-(3/2)k^2/k_0^2)$. In Smirnov's RFG method, a Gaussian distribution with standard deviation of $k_0/2$ (while $k_0=1$) was chosen for k_i^n , so the spectrum of the resulted velocity field follows $E_2(k)$ or $E_4(k)$ (i.e., the Gaussian model).

Noting that the spectrum $E_1(k)$ or $E_3(k)$ has a non-zero value at and only at k_0 , which is a very flexible feature so that we can construct a spectrum with arbitrary shape as follows:

For any given 3D spectrum $E(k)$, it can be discretized into the combination of many single pieces of $E(k_m)$, that is

$$E(k) = \sum_{m=k_0}^{k_{\max}} E_m(k) = \sum_{m=1}^{k_{\max}} E(k_m)\delta(k-k_m) = \sum_{m=1}^{k_{\max}} \left(\frac{3}{2}v_m^2\right)\delta(k-k_m) \quad (10)$$

For each $E_m(k)$, its random fluctuating flow field can be generated according to Kraichnan's (1970) study,

$$u_{m,i} = \sum_{n=1}^N [p_i^{m,n} \cos(k_j^{m,n}x_j + \omega_{m,n}t) + q_i^{m,n} \sin(k_j^{m,n}x_j + \omega_{m,n}t)] \quad (11)$$

where $k_j^{m,n}$ is isotropically distributed on the surface of a sphere of radius k_m , and $\omega_{m,n} \in N(0, \omega_{m,n})$.

Here, $p_i^{m,n}$ and $q_i^{m,n}$ are needed to be determined according to $E(k_m)$, so that one has

$$u_{rms,m,i}^2 = \frac{1}{T} \int_0^T u_{m,i}^2 dt = \frac{2}{3} E_m(k_m) = \frac{2}{3} E(k_m) \quad (12)$$

i.e.,

$$\begin{aligned} \frac{1}{T} \int_0^T u_{m,i}^2 dt &= \frac{1}{T} \int_0^T \left\{ \sum_{n=1}^N [p_i^{m,n} \cos(k_j^{m,n}x_j + \omega_{m,n}t) + q_i^{m,n} \sin(k_j^{m,n}x_j + \omega_{m,n}t)] \right\}^2 dt \\ &= \frac{1}{T} \sum_{n=1}^N \int_0^T [p_i^{m,n} \cos(k_j^{m,n}x_j + \omega_{m,n}t)]^2 dt \\ &\quad + \frac{1}{T} \sum_{n=1}^N \int_0^T [q_i^{m,n} \sin(k_j^{m,n}x_j + \omega_{m,n}t)]^2 dt \\ &= \frac{1}{T} \sum_{n=1}^N [p_i^{m,n}]^2 \frac{T}{2} + \frac{1}{T} \sum_{n=1}^N [q_i^{m,n}]^2 \frac{T}{2} \\ &= \frac{1}{2} \sum_{n=1}^N [p_i^{m,n}]^2 + \frac{1}{2} \sum_{n=1}^N [q_i^{m,n}]^2 = \frac{2}{3} E(k_m) \end{aligned}$$

Summing the left and right hands for $i=1,2,3$, we have

$$\frac{1}{2} \sum_{n=1}^N \sum_{i=1}^3 [p_i^{m,n}]^2 + \frac{1}{2} \sum_{n=1}^N \sum_{i=1}^3 [q_i^{m,n}]^2 = 2E(k_m) \quad (13)$$

The above equation is expressed in vector form, i.e.,

$$\frac{1}{2} \sum_{n=1}^N |\mathbf{p}^{m,n}|^2 + \frac{1}{2} \sum_{n=1}^N |\mathbf{q}^{m,n}|^2 = 2E(k_m) \quad (14)$$

where $\mathbf{p}^{m,n}$ and $\mathbf{q}^{m,n}$ are the vector form of $p_i^{m,n}$ and $q_i^{m,n}$, respectively, which cannot be solved from Eq. (14) directly. But, if we choose

$$|\mathbf{p}^{m,n}| = \sqrt{a \frac{4E(k_m)}{N}} \quad (15)$$

$$|\mathbf{q}^{m,n}| = \sqrt{(1-a) \frac{4E(k_m)}{N}} \quad (16)$$

where a is a random number uniformly distributed between 0 and 1, then one has

$$\frac{1}{2} \sum_{n=1}^N |\mathbf{p}^{m,n}|^2 + \frac{1}{2} \sum_{n=1}^N |\mathbf{q}^{m,n}|^2 = \frac{1}{2} \frac{4E(k_m)}{N} \left[\sum_{n=1}^N a + \sum_{n=1}^N (1-a) \right] = 2E(k_m)$$

i.e. Eq. (14) and thus Eq. (12) are satisfied.

2.3. Synthesizing $\mathbf{u}(\mathbf{x}, t)$ for a homogeneous and isotropic turbulent flow field

Obviously, $\mathbf{u}(\mathbf{x}, t)$ can be synthesized from $\mathbf{u}_m(\mathbf{x}, t)$ as follows:

$$\begin{aligned} \mathbf{u}(\mathbf{x}, t) &= \sum_{m=k_0}^{k_{\max}} \mathbf{u}_m(\mathbf{x}, t) = \sum_{m=k_0}^{k_{\max}} \sum_{n=1}^N [\mathbf{p}^{m,n} \cos(\tilde{\mathbf{k}}^m \cdot \mathbf{n} \cdot \tilde{\mathbf{x}} + \omega_{m,n}t) \\ &\quad + \mathbf{q}^{m,n} \sin(\tilde{\mathbf{k}}^m \cdot \mathbf{n} \cdot \tilde{\mathbf{x}} + \omega_{m,n}t)] \end{aligned} \quad (17)$$

where $\mathbf{p}^{m,n}$ and $\mathbf{q}^{m,n}$ are determined below:

$$\mathbf{p}^{m,n} = \frac{\zeta \times \mathbf{k}^{m,n}}{|\zeta \times \mathbf{k}^{m,n}|} \sqrt{a \frac{4E(k_m)}{N}} \quad (18)$$

$$\mathbf{q}^{m,n} = \frac{\xi \times \mathbf{k}^{m,n}}{|\xi \times \mathbf{k}^{m,n}|} \sqrt{(1-a) \frac{4E(k_m)}{N}} \quad (19)$$

$$\tilde{\mathbf{x}} = \frac{\mathbf{x}}{L_s} \quad (20)$$

$$\tilde{\mathbf{k}}^m \cdot \mathbf{n} = \frac{\mathbf{k}^{m,n}}{k_0}, \quad |\mathbf{k}^{m,n}| = k_m \quad (21)$$

$$\omega_{m,n} \in N(0, 2\pi f_m), f_m = k_m U_{avg} \quad (22)$$

where ζ and ξ are vector form of ζ_i^n and ξ_i^n , respectively. f is wave frequency and U_{avg} is mean velocity. L_s is a length scale of turbulence and is used as a scaling factor for spatial correlation. It is worthy noting that in the RFG method (Smirnov et al., 2001), L_s is selected as l , and there is no further specification about its role. Here, we will prove that L_s is a very important parameter in the present method and in the RFG method to acquire the target spatial correlation. To demonstrate this, the spatial correlation operator is constructed as follows:

$$\begin{aligned} \mathbf{Sc}(\mathbf{x}, \mathbf{x}') &= \int_0^T \mathbf{u}(\mathbf{x}, t) \cdot \mathbf{u}(\mathbf{x}', t) dt \\ &= \int_0^T \left\{ \sum_{m=k_0}^{k_{\max}} \sum_{n=1}^N \left[\mathbf{p}^{m,n} \cos(\tilde{\mathbf{k}}^m \cdot \mathbf{n} \cdot \tilde{\mathbf{x}} + \omega_{m,n}t) \right. \right. \\ &\quad \left. \left. + \mathbf{q}^{m,n} \sin(\tilde{\mathbf{k}}^m \cdot \mathbf{n} \cdot \tilde{\mathbf{x}} + \omega_{m,n}t) \right] \right\} \\ &\quad \times \left\{ \sum_{m=k_0}^{k_{\max}} \sum_{n=1}^N \left[\mathbf{p}^{m,n} \cos(\tilde{\mathbf{k}}^m \cdot \mathbf{n} \cdot \tilde{\mathbf{x}}' + \omega_{m,n}t) \right. \right. \\ &\quad \left. \left. + \mathbf{q}^{m,n} \sin(\tilde{\mathbf{k}}^m \cdot \mathbf{n} \cdot \tilde{\mathbf{x}}' + \omega_{m,n}t) \right] \right\} dt \\ &= \int_0^T \left\{ \sum_{m=k_0}^{k_{\max}} \sum_{n=1}^N \left[(\mathbf{p}^{m,n})^2 \cos(\tilde{\mathbf{k}}^m \cdot \mathbf{n} \cdot \tilde{\mathbf{x}} + \omega_{m,n}t) \cos(\tilde{\mathbf{k}}^m \cdot \mathbf{n} \cdot \tilde{\mathbf{x}}' + \omega_{m,n}t) \right. \right. \\ &\quad \left. \left. + (\mathbf{q}^{m,n})^2 \sin(\tilde{\mathbf{k}}^m \cdot \mathbf{n} \cdot \tilde{\mathbf{x}} + \omega_{m,n}t) \sin(\tilde{\mathbf{k}}^m \cdot \mathbf{n} \cdot \tilde{\mathbf{x}}' + \omega_{m,n}t) \right] \right\} dt \\ &= \sum_{m=k_0}^{k_{\max}} \sum_{n=1}^N \left[(\mathbf{p}^{m,n})^2 \cos[\tilde{\mathbf{k}}^m \cdot \mathbf{n} \cdot (\tilde{\mathbf{x}} - \tilde{\mathbf{x}}')] \frac{T}{2} + (\mathbf{q}^{m,n})^2 \cos[\tilde{\mathbf{k}}^m \cdot \mathbf{n} \cdot (\tilde{\mathbf{x}} - \tilde{\mathbf{x}}')] \frac{T}{2} \right] \\ &= \sum_{m=k_0}^{k_{\max}} \sum_{n=1}^N \left[(\mathbf{p}^{m,n})^2 \cos[\tilde{\mathbf{k}}^m \cdot \mathbf{n} \cdot (\tilde{\mathbf{x}} - \tilde{\mathbf{x}}')] \frac{T}{2} + (\mathbf{q}^{m,n})^2 \cos[\tilde{\mathbf{k}}^m \cdot \mathbf{n} \cdot (\tilde{\mathbf{x}} - \tilde{\mathbf{x}}')] \frac{T}{2} \right] \\ &= \sum_{m=k_0}^{k_{\max}} \left\{ \frac{2TE(k_m)}{N} \sum_{n=1}^N \cos[\tilde{\mathbf{k}}^m \cdot \mathbf{n} \cdot \frac{(\mathbf{x} - \mathbf{x}')}{L_s}] \right\} \end{aligned} \quad (23)$$

According to Eq. (23), for a given $E(k_m)$, different L_s will lead to different change rates of $\mathbf{Sc}(\mathbf{x}, \mathbf{x}')$, i.e., it has an effect of adjusting the spatial correlation between two points, which provides a way to obtain the required spatial correlation in the generated flow field. It should be noted that there are multiple choices for L_s . In the next section, several choices of L_s and their effects on spatial

correlations of the resulted fluctuating velocity field will be discussed.

2.3.1. Synthesizing $\mathbf{u}(\mathbf{x}, t)$ for a inhomogeneous and anisotropic turbulent flow field

As mentioned previously, the scaling and orthogonal transformation operations used in Smirnov's RFG method can be applied in the present method to generate an anisotropic turbulent flow field, i.e., given an anisotropic velocity correlation tensor, Eqs. (7) and (8) can be applied to $\mathbf{u}(\mathbf{x}, t)$ generated by Eqs. (17)–(21) to obtain a fluctuating velocity field with correlation approaching the anisotropic target value. However, this is not an effective way to generate a realistic inhomogeneous and anisotropic fluctuating velocity field. This is due to the fact that only the amplitude of velocity fluctuation is rescaled with the given anisotropic velocity correlation by the scaling and orthogonal transformation operations, the spectrum of the resulted velocity field may not be changed, which may still be spatially isotropic rather than anisotropic. But, in a realistic inhomogeneous and anisotropic turbulent flow field, its spectrum may also be spatially anisotropic. Obviously, the scaling and orthogonal transformation operations are incapable of solving such a problem.

To solve this problem, a more comprehensive method for dealing with inhomogeneity and anisotropy is proposed herein. It should be noted that in the construction of a homogeneous and isotropic turbulent flow field (Eq. (17)), $\mathbf{p}^{m,n}$ and $\mathbf{q}^{m,n}$ are responsible for the distribution of a 3D energy spectrum $E(k_m)$ in three spatial coordinate axes. Since $\mathbf{p}^{m,n}$ and $\mathbf{q}^{m,n}$ are constructed based on space wave number $\mathbf{k}^{m,n}$ and 3D normal random number ζ and ξ , the statistical distribution of $\mathbf{k}^{m,n}$ essentially determines how a 3D energy spectrum $E(k_m)$ is distributed in space. In the case of homogeneous and isotropic flow field, $\mathbf{k}^{m,n}$ is isotropically distributed on the surface of a sphere, hence the energy is uniformly distributed in space, and an identical spectrum will be obtained in the three principle axes. For inhomogeneous and anisotropic spectra, the distribution of $\mathbf{k}^{m,n}$ is needed to be changed according to the degree of inhomogeneity and anisotropy. But it is difficult to directly determine the distribution of $\mathbf{k}^{m,n}$ based on the degree of inhomogeneity and anisotropy. An aligning and remapping procedure is adopted below to solve this problem.

First, according to Eq. (12), we can make the components of $\mathbf{p}^{m,n}$ and $\mathbf{q}^{m,n}$ be aligned with the energy spectrum along the principle axis before determination of $\mathbf{k}^{m,n}$, i.e.,

$$[p_i^{m,n}]^2 + [q_i^{m,n}]^2 = \frac{4}{3N} E(k_m) = \frac{4}{N} E_i(k_m) \quad (24)$$

where $E_i(k_m)$ is the energy spectrum along direction i , and one has

$$E(k_m) = \sum_{i=1}^3 E_i(k_m) \quad (25)$$

Then, we have

$$p_i^{m,n} = \text{sign}(r_i^{m,n}) \sqrt{\frac{4}{N} E_i(k_m) \frac{(r_i^{m,n})^2}{1 + (r_i^{m,n})^2}} \quad (26)$$

$$q_i^{m,n} = \text{sign}(r_i^{m,n}) \sqrt{\frac{4}{N} E_i(k_m) \frac{1}{1 + (r_i^{m,n})^2}} \quad (27)$$

where $r_i^{m,n}$ is a random number, which will be picked independently from a three dimensional normal distribution with mean of 0 and standard deviation of 1. It is clear that such operations can

directly determine the energy distribution in each axis according to the target spectrum in the same direction. Summing Eq. (24) in the three principle axes will yield the same equation with Eq. (14), which means that the general energy spectrum is still kept unchanged.

Once the target $\mathbf{p}^{m,n}$ and $\mathbf{q}^{m,n}$ are obtained, the distribution of $\mathbf{k}^{m,n}$ can be remapped on the surface of the sphere according to the following equations:

$$\mathbf{k}^{m,n} \cdot \mathbf{p}^{m,n} = 0 \quad (28)$$

$$\mathbf{k}^{m,n} \cdot \mathbf{q}^{m,n} = 0 \quad (29)$$

$$|\mathbf{k}^{m,n}| = k_m \quad (30)$$

These equations will make the divergence-free condition be strictly satisfied and the uniform distribution of $\mathbf{k}^{m,n}$ on the surface of the sphere adjusted with the target spectrum of inhomogenous and anisotropic turbulence. In fact, this procedure is a general approach. The homogenous and isotropic turbulence can also be generated if the input $E_i(k_m)$ are identical in the three directions.

Besides, since the key elements of the present method involve the discretizing and synthesizing procedures for generation of a random flow filed, for convenience of depiction, the proposed approach is called as discretizing and synthesizing random flow generation (DSRFG) method.

3. Validation

3.1. Validation and sensitivity study of key parameters

3.1.1. Validation of a homogeneous isotropic turbulent flow field

The first validation example is to examine the performance of the proposed method to generate a homogeneous isotropic turbulent flow field. The physical turbulence statistical parameters are $I_u = I_v = I_w = I = 8\%$, where I_u , I_v , I_w are turbulence intensity in x , y , z (longitudinal, lateral and vertical) direction, respectively; and $L_u = L_v = L_w = L = 0.3$ m, where L_u , L_v , L_w are the turbulence integral length scales in the three coordinate direction, respectively. The mean wind speed is $U_{avg} = 14$ m/s. The energy spectrum of fluctuating wind speed in each direction is assumed to be described by the von Karman model (Simiu and Scanlan, 1996), i.e.,

$$S_u(f) = S_v(f) = S_w(f) = \frac{4(IU_{avg})^2(L/U_{avg})}{[1 + 70.8(fL/U_{avg})^2]^{5/6}} \quad (31)$$

So the 3D energy spectrum is given by

$$E(k) = E(kU_{avg}) = E(f) = \frac{3}{2} S_u(f) \quad (32)$$

Fig. 3 shows the resulted spectra generated by the present DSRFG method and comparison with the target spectrum. Obviously, they are in good agreement. Samples of fluctuating wind speed are shown in Fig. 4 and those generated by Smirnov's RFG method are also displayed in the figure for comparison purposes. It can be seen from this figure that higher frequency wind speed fluctuations are generated by the present method, which is in accordance with the spectra shown in Fig. 3. In contrast, the frequency content of wind speed fluctuations generated by the RFG method is much lower than that produced by the present method, since the spectra generated by the RFG method decayed rapidly in high frequency range, as shown in Fig. 2.

Fig. 5 shows the spatial correlations of the generated turbulent flow field. Here the spatial correlations generated by the RFG and DSRFG are compared in Fig. 5(a), while those generated by the

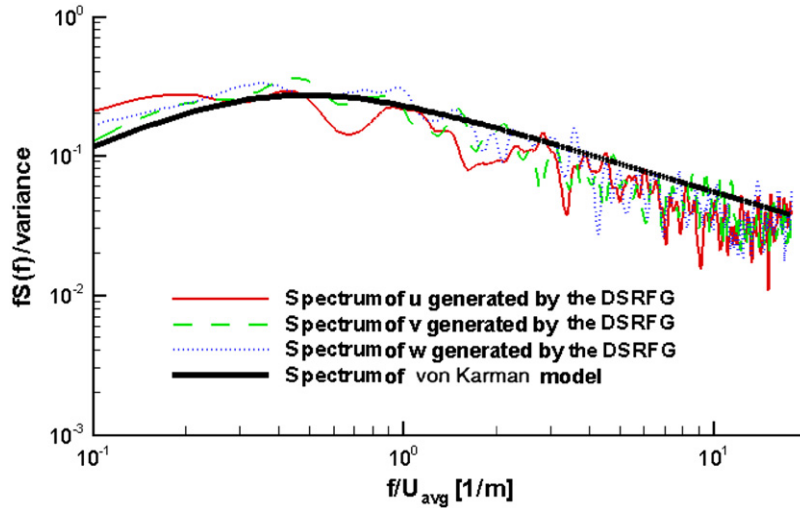


Fig. 3. Comparison of the spectra by the DSRFG method and the target spectrum ($I_u=8\%$, $L_u=0.3$ m).

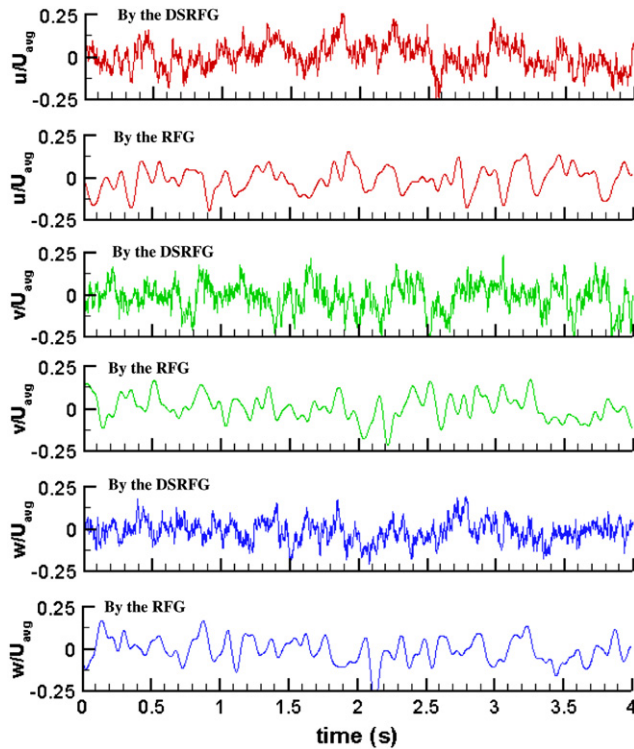


Fig. 4. Comparison of wind velocity samples simulated by the RFG and DSRFG methods ($I_u=8\%$, $L_u=0.3$ m).

DSRFG method with three different turbulence integral length scales chosen as the spatial scaling factor are shown in Fig. 5(b). The first choice is the turbulence integral length scale l used in Smirnov's RFG method, which is estimated as $l=(C_\mu)^{0.75} k^{1.5}/\varepsilon=0.13$ m, where k is the turbulence kinetic energy, ε is the dissipation rate, $C_\mu=0.09$. k can be estimated by $k=3/2(IU_{avg})^2$ while ε is calculated from the spectral curve in inertial subrange as $\varepsilon=a^{-1.5}\kappa^{5/2}E_u(\kappa)^{3/2}$, where κ is the wavelength in inertial subrange, $E_u(\kappa)$ is energy spectral intensity, $a=0.5\text{--}0.6$. The second choice is the integral length scale of turbulence L , which is provided directly. The third choice is $C_L l$, where C_L is a constant between 1 and 2. The results for the different choices of L_s are compared with the target, which is estimated by the following

equation (Hemon and Santi, 2007):

$$Sc_{i,j} = \sum_l \sqrt{S_{u,i}(f_l)S_{u,j}(f_l)} \gamma_u^v(f_l) = \sum_l \sqrt{S_{u,i}(f_l)S_{u,j}(f_l)} \exp\left[\frac{-C_u^y |y_i - y_j| f}{U_{avg}}\right] \quad (33)$$

where $\gamma_u^v(f_l)$ is coherence function approximated by an exponential function. C_u^y is decay coefficient, which is between 10 and 12 in the present calculation.

Comparing the results shown in Fig. 5(a), it is clear that the spatial correlation generated by the RFG is erroneous in shape of correlation curve as compared with the target and that generated by the DSRFG. Besides, it decreases rapidly with distance, which means less spatial correlation of the generated turbulent flow field. For the DSRFG, the correlation is in good agreement with the target exponent function, although it does not exactly match the target. Comparing the results of the three different choices of the spatial scaling factor, choice of 1.5L seems to yield the best result, while that proposed by Smirnov et al. (2001) leads to the worst result. It should be noted that 1.5 is not a universal constant. It can be adjusted according to different targets.

3.1.2. Validation of an inhomogeneous anisotropic turbulent flow field

Realistic turbulence is always inhomogeneous and anisotropic, for example, turbulent wind flows in atmospheric boundary layer. The spectra of the three principal velocity components are usually described by (Simiu and Scanlan, 1996)

$$S_u(f) = \frac{4(I_u U_{avg})^2 (L_u/U_{avg})}{[1 + 70.8(f L_u/U_{avg})^{2/5}]^{1/6}} \quad (34)$$

$$S_v(f) = \frac{4(I_v U_{avg})^2 (L_v/U_{avg}) (1 + 188.4(2f(L_v/U_{avg}))^2)}{[1 + 70.8(2f L_v/U_{avg})^{2/11}]^{1/6}} \quad (35)$$

$$S_w(f) = \frac{4(I_w U_{avg})^2 (L_w/U_{avg}) (1 + 188.4(2f(L_w/U_{avg}))^2)}{[1 + 70.8(2f L_w/U_{avg})^{2/11}]^{1/6}} \quad (36)$$

For turbulence parameters $I_u=8\%$, $I_v=16\%$, $I_w=24\%$, $L_u=0.6$ m, $L_v=0.3$ m, $L_w=0.1$ m (these values are selected arbitrarily), Fig. 6 shows the differences of the spectra $S_u(f)$, $S_v(f)$ and $S_w(f)$, illustrating that the turbulent flow for this case is obviously anisotropic.

The anisotropic turbulent flow is generated by the scaling and orthogonal transformation technique incorporated in the DSRFG

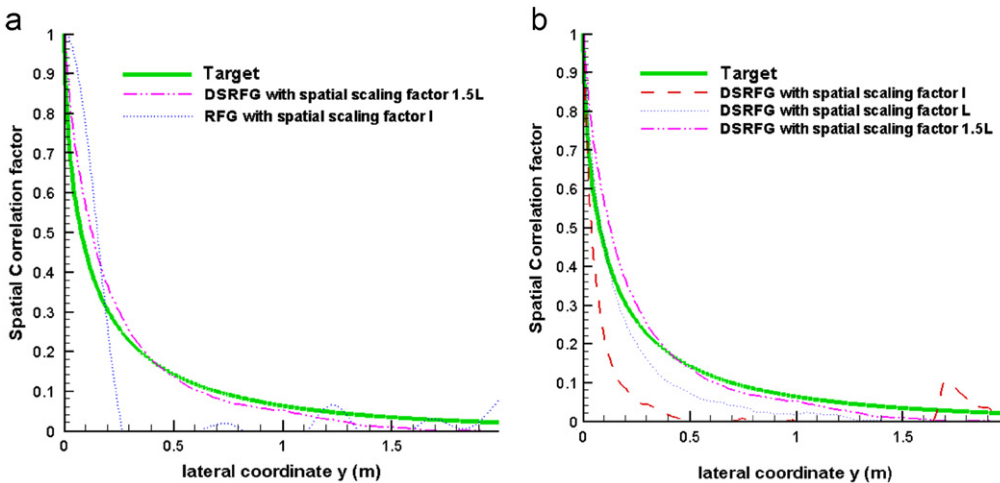


Fig. 5. Comparison of spatial correlation generated by the RFG and DSRFG methods ($I_u=8\%$, $L_u=0.3$ m). (a) RFG vs. DSRFG and (b) DSRFG with different L_s .

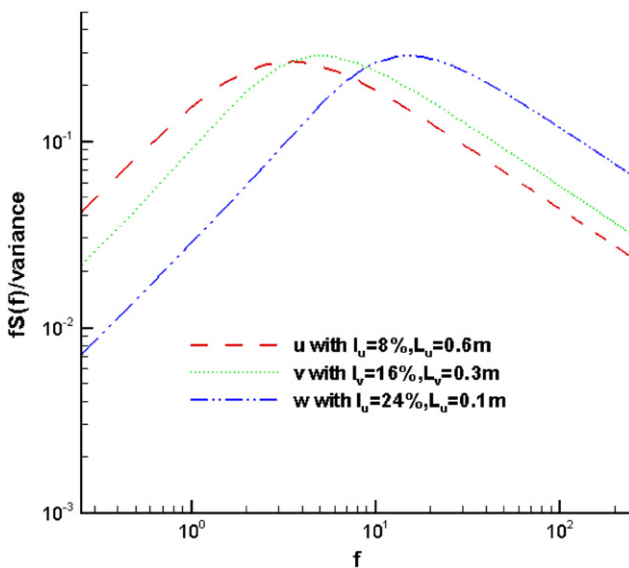


Fig. 6. Target spectra for inhomogeneous and anisotropic turbulence.

method to account for the anisotropic features. The anisotropic velocity correlation tensor is given by

$$\begin{pmatrix} r_{uu} & 0 & 0 \\ 0 & r_{vv} & 0 \\ 0 & 0 & r_{ww} \end{pmatrix} = \begin{pmatrix} (I_u U_{avg})^2 & 0 & 0 \\ 0 & (I_v U_{avg})^2 & 0 \\ 0 & 0 & (I_w U_{avg})^2 \end{pmatrix} \quad (37)$$

Comparison of the resulted spectra with the target spectra is shown in Fig. 7. The rms value of each spectrum is also compared with the corresponding target value in Table 1. Then the flow field is also generated by using the aligning and remapping technique incorporated in the DSRFG method, the simulated results are compared with those by the scaling and orthogonal transformation technique, as shown in Figs. 8–11 and Table 1. It is apparent that:

- (1) The resulted rms value of each fluctuating component simulated by both the techniques is in good agreement with the corresponding target value, except that the scaling and orthogonal technique slightly over-predicted that of the v component (σ_v), suggesting that the two methods can simulate the anisotropy of I_u , I_v and I_w correctly.

- (2) As discussed previously, the scaling and orthogonal technique is incapable of dealing with the case of anisotropy of spectra. The results shown in Fig. 7 confirm the conclusion again. Here it is observed that the anisotropy of spectra in different spatial directions cannot be properly simulated by the scaling and orthogonal technique. Relatively large discrepancies exist between the simulated spectra and the target spectra, especially for the w component, as shown in Fig. 7. On the contrary, the spectra simulated by the aligning and remapping technique agree with the target spectra well, as shown in Fig. 8, illustrating that it has good capability of dealing with the anisotropy of spectra.
- (3) The spatial correlations of the flow fields simulated by the two methods are shown in Figs. 9–11 for comparison purposes. The target correlations of the v component and the w component are calculated by Eq. (33) with $S_u(f)$ replaced by $S_v(f)$ and $S_w(f)$ for y and z direction, respectively. In the simulation using the scaling and orthogonal technique, $1.5L_u$, $1.5L_v$ and $1.5L_w$ were used as the scaling factor for the x , y and z spatial coordinate, respectively, while in the computation using the aligning and remapping technique, a single equivalent scale factor constructed by $\sqrt{L_u^2 + L_v^2 + L_w^2}$ was used, since the distribution of $\mathbf{k}^{m,n}$ has been remapped with consideration of spatial anisotropy of spectra and anisotropy of turbulence integral length scale. The results generated by the aligning and remapping technique show that the simulated spatial correlations in the x , y and z direction are in better agreement with the target values.

3.1.3. Sensitivity study of key parameters

The key parameters in the DSRFG method include N (sampling number for each wave number k_m) and sampling frequency $f_{max} = 1/(2dt)$. Compared with the RFG method, the computational complexity of the DSRFG method is measured by $f_{max} \cdot N$, which means that the computational cost of the DSRFG method is f_{max} times more than that of the RFG method. Hence, f_{max} should be chosen carefully to avoid increasing computational cost. In this study, $N=100$ and $f_{max}=250$ ($dt=0.002$ s) are chosen as default, no statistically significant deviation was observed for $N > 100$. In the present study, $f_{max}=500$ ($dt=0.001$ s) was used and the parallel computation was implemented, since the simulation process for generation of turbulent flow at each point is independent.

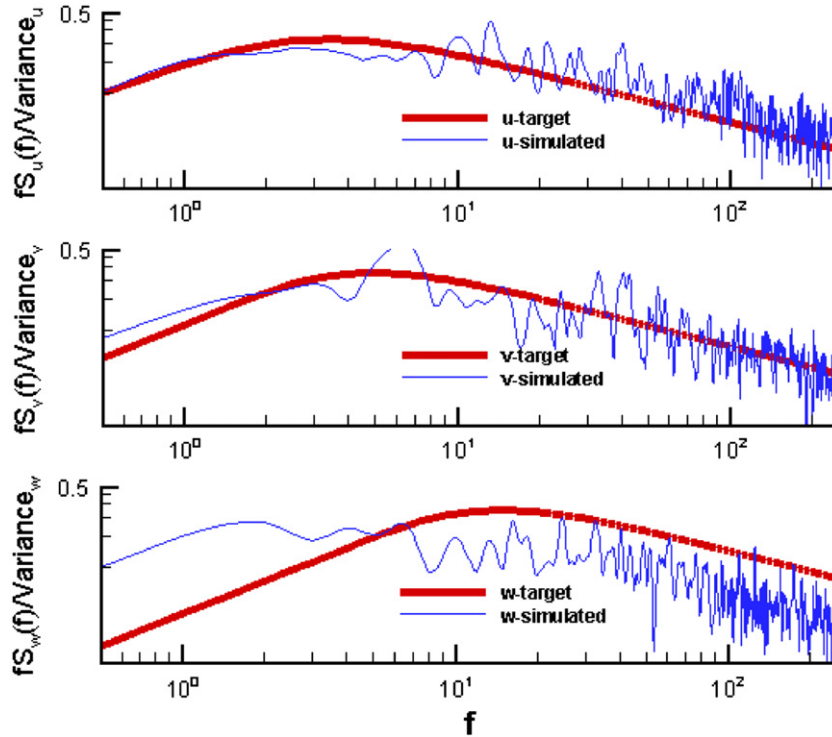


Fig. 7. Comparison of the spectra generated by the DSRFG using the technique of scaling and orthogonal transformation with the target spectra.

Table 1

Comparison of standard deviations of flow fields simulated by the DSRFG with different anisotropy treating techniques.

	σ_u	σ_v	σ_w
Scaling & transformation	0.9968	2.44	2.9956
Aligning & remapping	0.95	1.9987	3.08
Target	1.12	2.24	3.36

3.2. Application of the present inflow turbulence generation method to LES

As discussed previously, generation of a random flow field as inflow boundary condition that satisfies the von Karman spectrum or a reasonable spectrum for wind flow in atmospheric boundary layer is of great significance in CWE practices. In this section, the DSRFG method is used to generate a fluctuating wind velocity field as inflow boundary condition for simulation of wind loads on a tall building model by LES. The building model considered in the present study is a square prism with sharp edges, as schematically shown in Fig. 12. For comparison purposes, the RFG method proposed by Smirnov et al. (2001) was also used in the computation. The RFG method has been incorporated in the commercial software FLUENT named as *Spectral Synthesizer* (Fluent.Inc, 2003). The DSRFG method developed in the present study was added into FLUENT through a user defined function (UDF).

The wind tunnel test of this building model was conducted by Reinhold (1977), in which the wind velocity and turbulence statistical parameters of incident flow in simulated atmospheric boundary layer are listed in Table 2.

Computational domain, coordinate definition and boundary conditions for the present simulation study are shown in Fig. 13, in which the computational domain covers $28B$ (B is the width of

the building model) in streamwise (X) direction ($-6 < x/B < 32$), $16B$ in lateral (Y) direction ($-8 < y/B < 8$) and $2H$ (H is the building model height) in vertical (Z) direction, with a blockage ratio less than 3%. Compared with the guidelines provided by AIJ (Architectural Institute of Japan) and COST (European Cooperation in the Field of Scientific and Technical Research) (Yoshihide et al., 2008), the selected height of the computational domain is lower than that (5 H) recommended. However, the present results show that it is still acceptable since Fig. 20 shows that relatively uniform mean velocity contour lines are presented on the top of the computational domain above the building model, which implies that the effect of the building blockage on the computational flow field around the building is not significant.

The incident wind angle considered in the simulation study was zero (incident wind flow was normal to one of the building model surfaces). The computational grid arrangements are shown in Fig. 14. Reynolds number based on the approaching wind speed and the width of the building model was in the range from 5.9×10^4 to 1.1×10^5 , this implies that the boundary layer regions need fine grid points clustered near the building model surface. In consideration of computational resource and efficiency, the first point near the building model surface was chosen to be $0.05B$, with the corresponding wall unit y^+ about 30–80 ($y^+ = \rho u y / \mu$), which is suitable for wall function. The grid was non-uniformly distributed but carefulness was taken to avoid large stretching in the neighborhood region of the building model for reducing cutoff error of wave number in LES. In y direction on the horizontal $x-y$ plane, 40 uniformly spaced grid points were clustered near the building model surface with grid size of $0.05B$ and 44 points were distributed in the left domain with a stretching ratio of 1.15. In x direction, 60 grid points were distributed from inlet to the building model surface, with 20 points uniformly spaced ($0.05B$) near the building model surface and 40 points non-uniformly spaced to the inlet (stretching ratio 1.05). In the wake zone of the computational domain, 40 uniform-spaced points encompassing

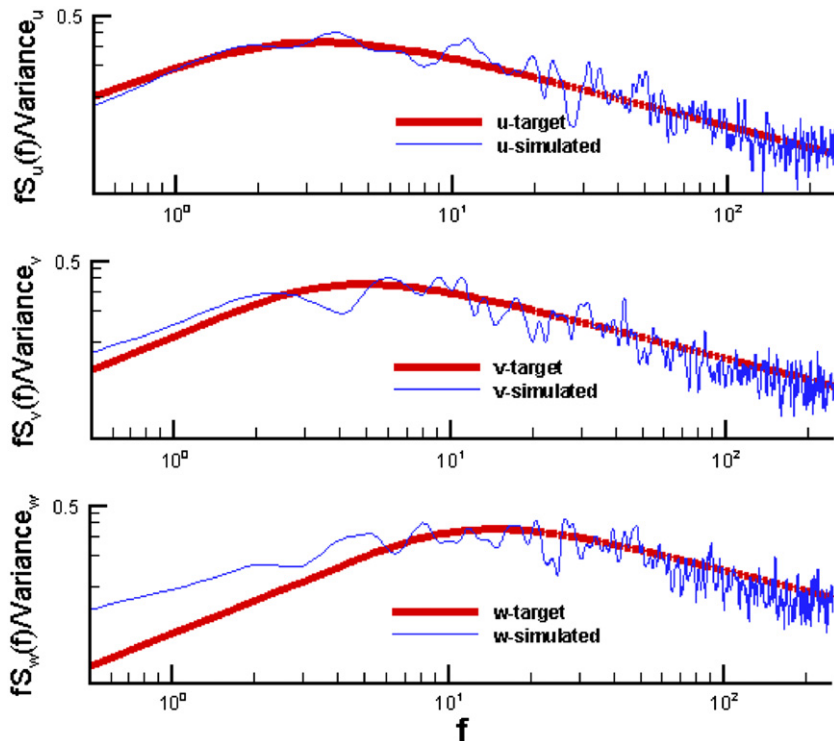


Fig. 8. Comparison of the spectra generated by the DSRFG using the technique of aligning and remapping with the target spectra.

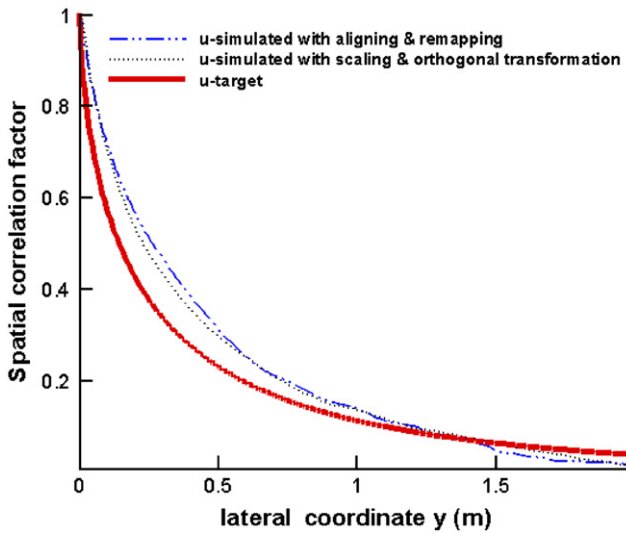


Fig. 9. Comparison of spatial correlation generated by the DSRFG using different anisotropy techniques (u component) with the target.

$2B$ of the building model were distributed near the building model surface and 80 points were stretched far away with a ratio of 1.05. In the direction of height (z), 70 points were distributed with the points clustered near the ground surface and the top surface of the building model (stretching ratio of 1.05). Totally, about 147,000 3D grid elements were generated in the present simulation.

The Pressure Implicit with Splitting of Operators (PISO) algorithm was adopted in the present simulation. The PISO involves one predictor step and two corrector steps and can be regarded as an extension of Semi-Implicit Method for Pressure-Linked Equations (SIMPLE), with a further corrector step to

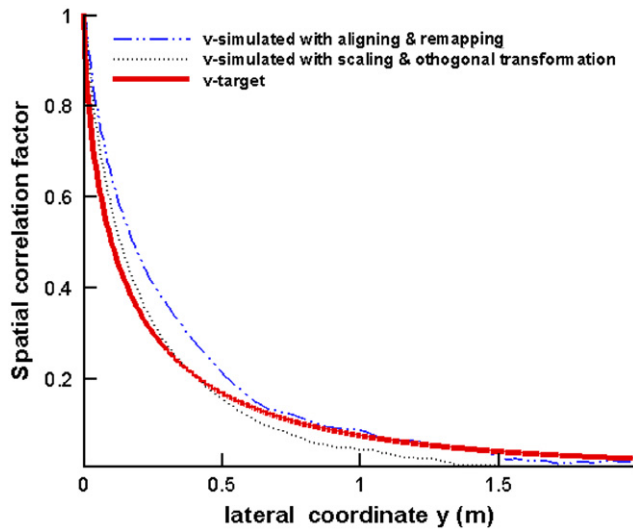


Fig. 10. Comparison of spatial correlation generated by the DSRFG with different anisotropy techniques (v component) with the target.

enhance it. The PISO is a pressure–velocity calculation procedure developed for the non-iterative computation of unsteady compressible flows. Therefore, the PISO has better performance in unsteady flow simulation than the SIMPLE series algorithm (Issa, 1986). The bounded central difference was used to discretize the convective terms of momentum equations for its relative low diffusivity. The second order implicit scheme was used for time discretization. The subgrid-scale (SGS) model chosen in this study is the dynamic Smagorinsky–Lilly model (Lilly, 1992).

The computation was performed in a supercomputer at the supercomputer center of Shanghai. Totally 12 CPUs were used in parallel for the simulation. The numerical time step was restricted

to 1×10^{-3} s. 78 CPU seconds were needed for each time step (about 30 CPU seconds for 5 sub iteration; 28 CPU seconds for the computation using the DSRFG; 20 CPU seconds for monitoring the forces). Totally about 86 CPU hours were spent for 4000 time steps. The statistical averaging of the simulated flow field was taken for the last 2000 steps (2 seconds). For the LES using the RFG for the inflow turbulence generation, about 30% computational time was saved due to less computational cost of the RFG.

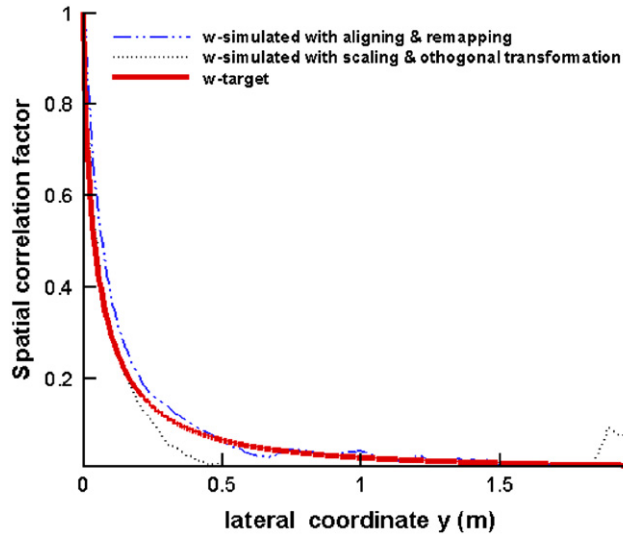


Fig. 11. Comparison of spatial correlation generated by the DSRFG with different anisotropy techniques (w component) with the target.

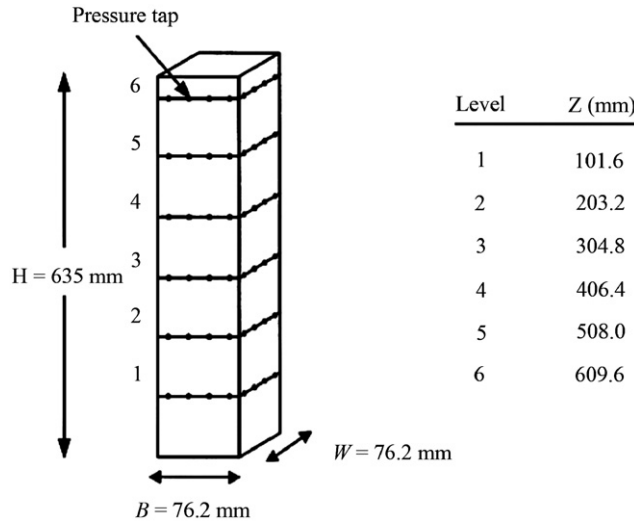


Fig. 12. A building model and experimental arrangements in wind tunnel test (Reinhold, 1977).

Table 2
Inflow wind boundary conditions in the wind tunnel test (Reinhold, 1977).

Level	Elevation (m)	Velocity (m/s)	Turbulence intensity (%)	Turbulence length scale	Reynolds numbers ($\rho UB/\mu$)
1	0.1016	10.1	27.71	0.2211	59,000
2	0.2032	13.0	23.13	0.2766	75,000
3	0.3048	15.1	18.12	0.3048	88,000
4	0.4064	16.8	13.69	0.3052	98,000
5	0.5080	18.3	10.25	0.2740	110,000
6	0.6096	19.5	8.13	0.2345	110,000

The inlet mean wind speed profile is described by a power law function as follows:

$$\frac{U}{U_H} = \left(\frac{Z}{Z_H} \right)^a \quad (38)$$

where a is the exponent of the mean wind speed profile, which was 0.37 determined by the data listed in Table 2. U_H is the mean wind speed at the height of the building model, which was 19.8 m/s.

When the RFG method is used to generate the inlet fluctuating velocity field, the kinetic energy of turbulence k and its dissipation rate ε at the inlet section need to be determined to calculate the characteristic length scale (l) and time scale (τ) of turbulence, as discussed previously. Here they are estimated by the method presented in Section 3.1.

Fig. 15 shows comparison of longitudinal fluctuating velocity spectra simulated by the two methods, at the height equivalent to the level 6 on the building model. It is clear that the spectrum determined by the present DSRFG method agrees with the von Karman spectrum well, while the spectrum obtained by the RFG method decays too fast in the inertial subrange. Fig. 16 shows the spatial correlations of wind speed simulated by the two methods. The target correlation is estimated by Eq. (33) with $C_u^y=12$ and the spatial scaling factor for DSRFG method is 1.5L. As discussed previously, choosing l as the spatial scaling factor in the RFG method leads to low spatial correlation in the generated random fluctuating wind field, which implies the velocity fluctuation is caused by a kind of initial disturbance rather than real turbulence eddies (Schluter et al., 2004). This phenomenon is further

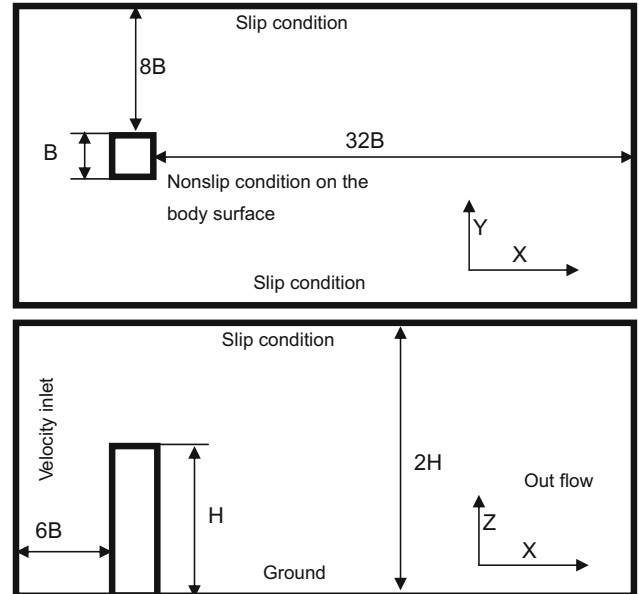


Fig. 13. Computational domain and boundary conditions.

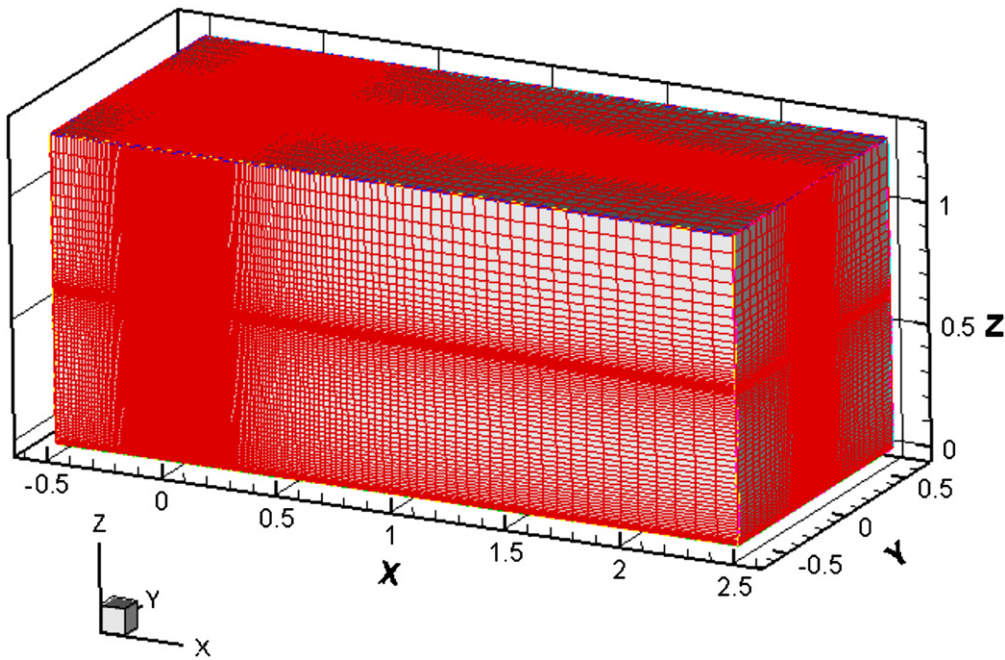


Fig. 14. Computational grid.

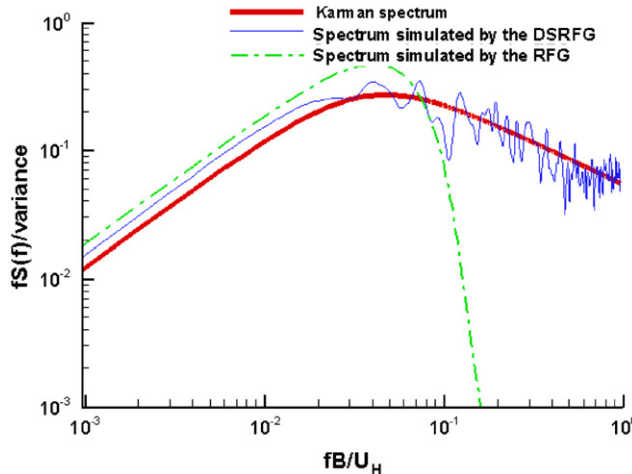


Fig. 15. Comparison of the spectra generated by the RFG and DSRFG methods with the target spectrum.

demonstrated in Fig. 17, in which much more eddies are generated at the inflow boundary by the present DSRFG method than the RFG method.

The along-wind force F_x , across-wind force F_y and torsional moment M at each level of the building model were recorded at each time step of the simulation. Then the time histories of F_x , F_y and M were input into MATLAB software to obtain their rms values (σ_{F_x} , σ_{F_y} and σ_M) and power spectra. Table 3 lists comparison of rms coefficients at different levels of the building model with the available experimental results (Reinhold, 1977). These coefficients are defined as $C_{\sigma_{F_x}} = \sigma_{F_x}/(1/2U_h^2BH_{Level})$, $C_{\sigma_{F_y}} = \sigma_{F_y}/(1/2U_h^2BH_{Level})$, and $C_{\sigma_M} = \sigma_M/(1/2U_h^2B^2H_{Level})$. As shown in Table 3, $C_{\sigma_{F_x}}$, $C_{\sigma_{F_y}}$ and C_{σ_M} predicted by the RFG method are all smaller than the experimental results, especially $C_{\sigma_{F_y}}$ and C_{σ_M} are about half of the experimental data. On the contrary, the accuracy of these rms coefficients is enhanced significantly by the present DSRFG method. They are very close to

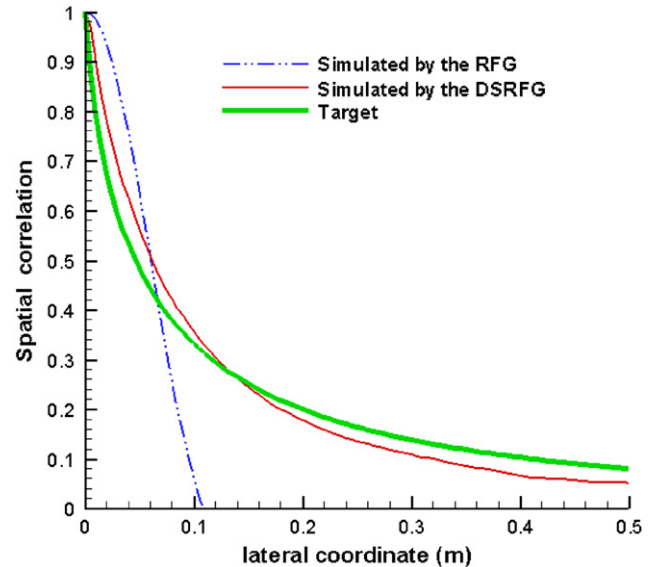


Fig. 16. Comparison of spatial correlation generated by the RFG and DSRFG methods with the target.

the experimental results, except 20–70% over-prediction of C_{σ_M} at the levels 4, 5 and 6. The over-prediction may be attributed to two reasons. First, only one line of pressure taps was installed on each level (totally 16 points), this may not be sufficient to precisely capture surface pressure distribution on each side surface, especially at the top level where complex 3D vortex evolution exists, which may lead to some errors in the measurements of torsional moment in the wind tunnel test (while in the numerical simulation, the pressures on each surface of the building model are integrated to obtain the torsional moment). Second, compared with the under-prediction case by the RFG method, over-prediction means that strong vortex shielding was captured in the simulation by the DSRFG method.

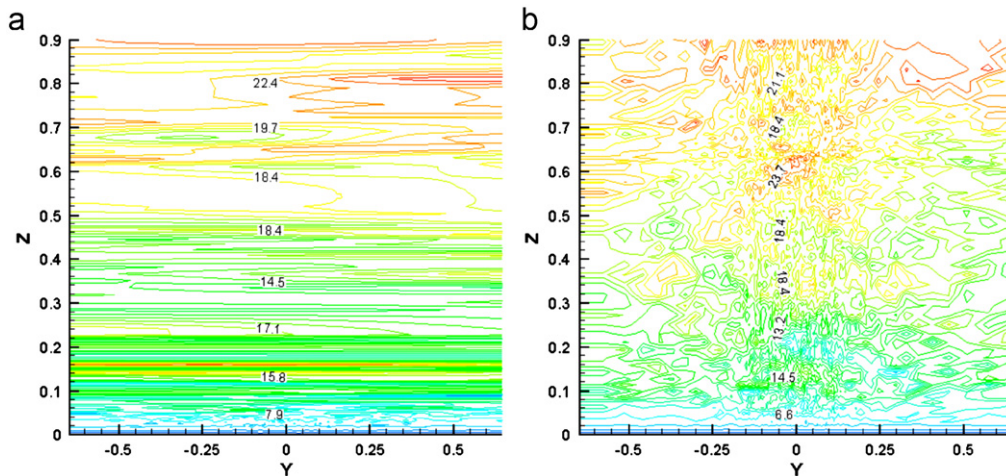


Fig. 17. Comparison of instantaneous velocity at the inflow boundary generated by the RFG and DSRFG methods. (a) By the RFG and (b) By the DSRFG.

Table 3

Comparison of rms values predicted by the RFG and DSRFG methods with experimental results (Reinhold, 1977).

Level	$C_{\sigma_{F_x}}$			$C_{\sigma_{F_y}}$			C_{σ_M}		
	Exp.	By the RFG	By the DSRFG	Exp.	By the RFG	By the DSRFG	Exp.	By the RFG	By the DSRFG
1	0.23	0.1612	0.1794	0.29	0.2548	0.2693	0.067	0.0477	0.0585
2	0.27	0.1843	0.2261	0.36	0.3145	0.3433	0.071	0.0474	0.0639
3	0.27	0.1931	0.2573	0.44	0.2737	0.4073	0.073	0.0355	0.0671
4	0.25	0.2231	0.2959	0.46	0.2142	0.4930	0.058	0.0244	0.0734
5	0.21	0.2283	0.2588	0.44	0.1876	0.4446	0.052	0.0246	0.0676
6	0.23	0.2486	0.2411	0.30	0.1368	0.3346	0.041	0.0197	0.0698

Fig. 18 shows comparison of vorticity magnitude contour in the simulated flow fields. First, in the upstream region of the building model where the inflow turbulence generation methods play a key role in generation of random eddies. More complex, random and larger vortices are observed in the flow field simulated by the DSRFG than that by the RFG. Second, for the results obtained by the DSRFG, larger vorticity magnitude is presented in the wake region of the building model as compared with that by the RFG. It is revealed from the simulation results and the associated comparisons that the random fluctuating velocity fields generated by the DSRFG method are much more similar to realistic turbulent wind flows in atmospheric boundary layer; thus will result in more realistic flow fields in downstream. This is actually due to the fact that more realistic spatial correlations were simulated by the DSRFG method, as discussed previously. Poor spatial correlations generated by the RFG make the velocity fluctuations caused by random disturbances to the flow field, as pointed out previously. Such spatial correlations will decay rapidly and have less effect on the turbulent flow field in downstream.

Fig. 19 shows the rms value of C_p , defined by $C_{p,rms} = P_{rms}/(1/2)\rho U_H^2$. It is observed from the figure that $C_{p,rms}$ in the separation and wake zones of the flow field simulated by the DSRFG method increases more quickly than that predicted by the RFG method, which is in accordance with the previous comparison regarding vorticity distributions. **Fig. 20** shows comparison of the mean velocity magnitude. Apparently, the location of vortex shedding in the wake region simulated by the RFG method is more downstream than that predicted by the DSRFG method and the separation angle near the corner of the sharp edge is also larger than that predicted by the DSRFG method. The reason for such differences should also be attributed

to the differences of spatial correlations in the turbulent flows generated by the two methods.

As discussed at the beginning of this paper, generation of inflow turbulence satisfying a spectrum such as the von Karman model is significant for numerical evaluation of wind effects on building and structures. The wind-induced forces and torsional moments acting on the building model surfaces are also calculated and analyzed in the present investigation. Figs. 21–23 show comparison of the time histories of the force coefficients predicted by the two methods at the position of $Z=0.8H$, in which the force coefficients are defined by $C_{F_x} = F_x/(1/2U_H^2BH_{level})$, $C_{F_y} = F_y/(1/2U_H^2BH_{level})$ and $C_M = M/(1/2U_H^2B^2H_{level})$. Figs. 24–26 show comparison of the normalized power spectral density functions of F_x , F_y and M between the numerical results and the experimental data, respectively. Based on those presented in these figures, it is observed that:

- (1) Higher frequency fluctuation of F_x was captured by the DSRFG method, as shown in **Fig. 21**, which is attributed to the increase of the power spectral density of F_x in the inertial subrange as shown in **Fig. 24**. It is encouraging to observe that the spectral density curves predicted by the DSRFG method are in better agreement with the experimental results as compared with those predicted by the RFG method, indicating that it is necessary to generate the inflow turbulence containing the inertial subrange of turbulence energy for obtaining realistic force spectra by LES.
- (2) As for F_y shown in **Fig. 22**, amplitude of fluctuating force coefficients predicted by the DSRFG method is about one time higher than that determined by the RFG method, which reveals that the locations of vortex shielding are moving

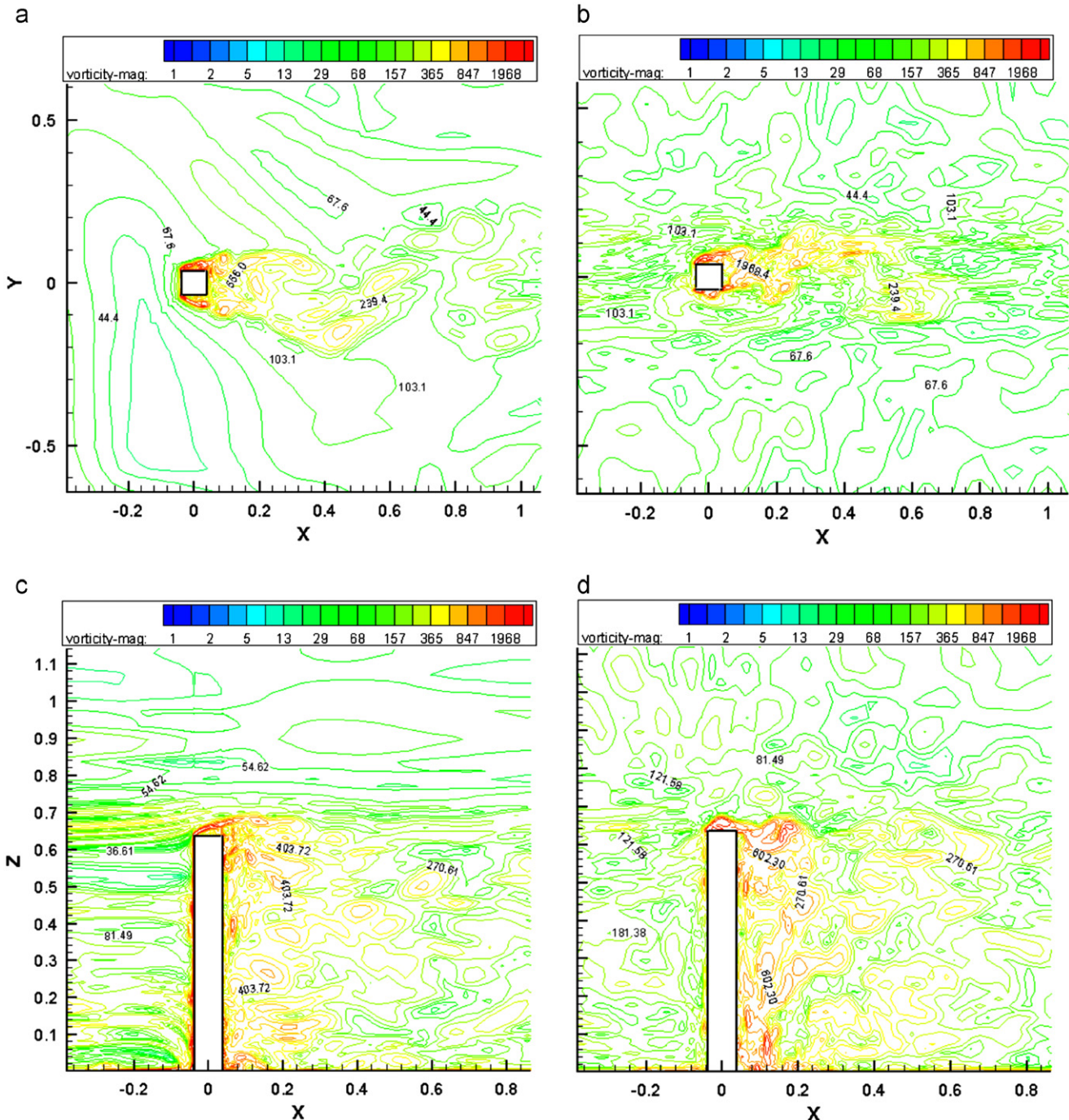


Fig. 18. Comparison of instantaneous vorticity magnitude contour predicted by the RFG and DSRFG methods. (a) By the RFG on x-y plane ($Z=0.8H$), (b) By the DSRFG on x-y plane ($Z=0.8H$), (c) By the RFG on x-z plane ($Y=0$) and (d) By the DSRFG on x-z plane ($Y=0$).

toward to the back face of the building model, inducing higher pressure variations near the side surfaces. This is a typical characteristic of the flow field around a bluff body when the turbulence intensity of the approaching flow is high. But this does not mean that the DSRFG method increases the turbulence intensity of the approaching flow. On the contrary, the good agreement of the power spectra density functions obtained by the DSRFG method and the wind tunnel test, as shown in Fig. 25, confirms that the DSRFG generates more realistic inflow turbulence than the RFG.

- (3) The similar observation with F_y was made for the torsional moments. This is because the torsional moments are mainly caused by the same mechanism (vortex shedding) with F_y . More importantly, the characteristic of dual peaks in the torsional spectrum was captured by the DSRFG method, while only one peak was simulated by the RFG method. Dual peaks occur when the turbulence intensity of wind flow is augmented in the wake region, which reveals again that the inflow turbulence was properly generated by the DSRFG.

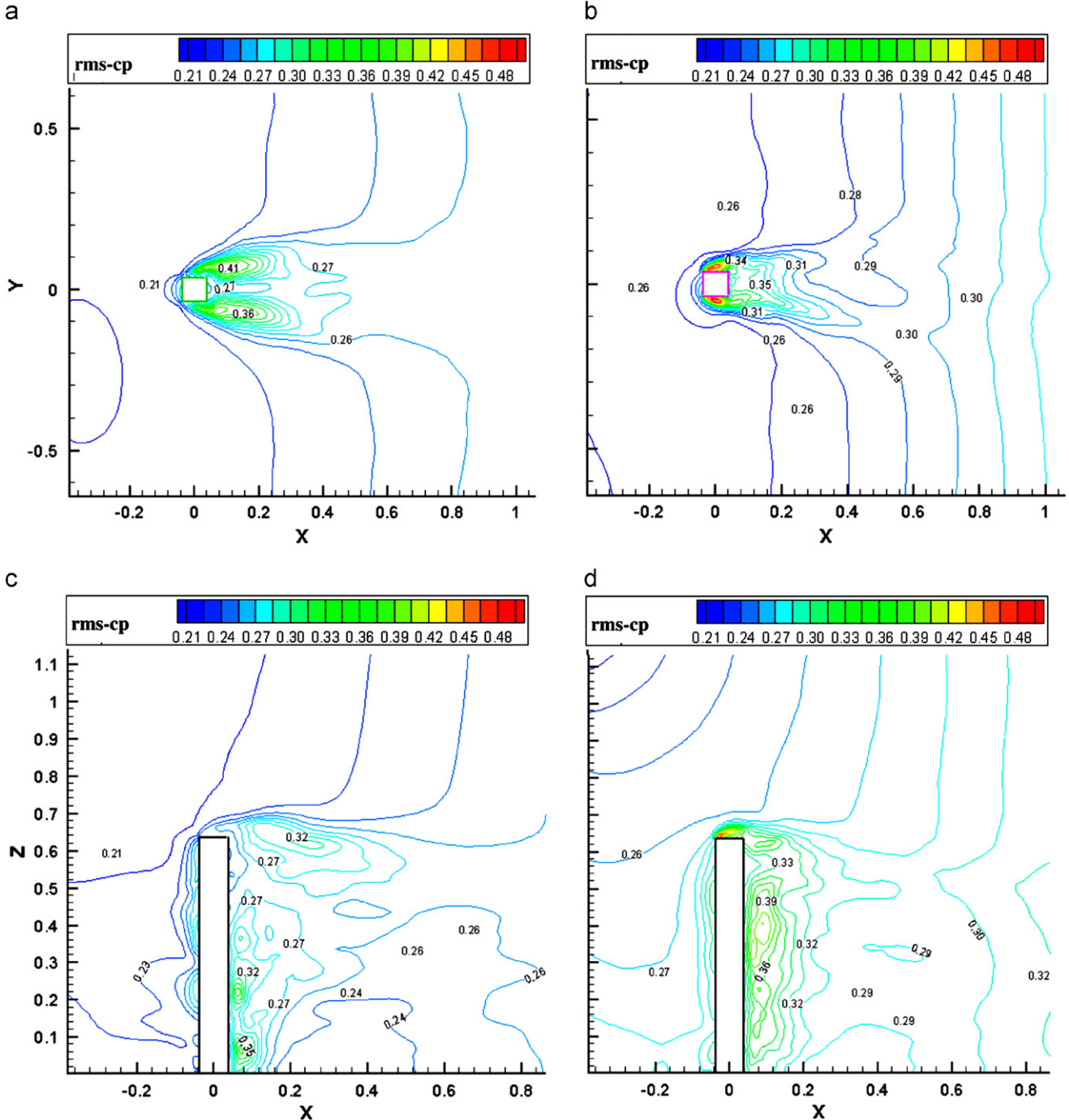


Fig. 19. Comparison of C_{rms} contour predicted by the RFG and DSRFG methods. (a) By the RFG on x-y plane ($Z=0.8H$), (b) By the DSRFG on x-y plane ($Z=0.8H$), (c) By the RFG on x-z plane ($Y=0$) and (d) By the DSRFG on x-z plane ($Y=0$).

4. Conclusions

A general inflow turbulence generator was presented based on the discretizing and synthesizing random flow generation (DSRFG) method and was validated in this study. This method can generate a fluctuating wind flow field satisfying any desired target spectrum by the technique of discretizing and synthesizing. The proposed approach was successfully extended to simulate inhomogeneous and anisotropic inflow turbulent flows by incorporating the aligning and remapping procedures. Through comparison with Smirnov's RFG inflow turbulence generation method, it was found that the

present DSRFG method has the following advantages:

- (1) It can rigorously guarantee inflow turbulence satisfying the divergence-free condition.
- (2) Inflow turbulent flow field with prescribed spatially anisotropic spectra can be well generated.
- (3) The spatial correlation of the generated flow field can be adjusted by choosing a proper spatial scaling factor.
- (4) Unlike existing methods, the DSRFG method is more suitable in implementing parallel computation, since the turbulence generation process for each point is independent. It helps to

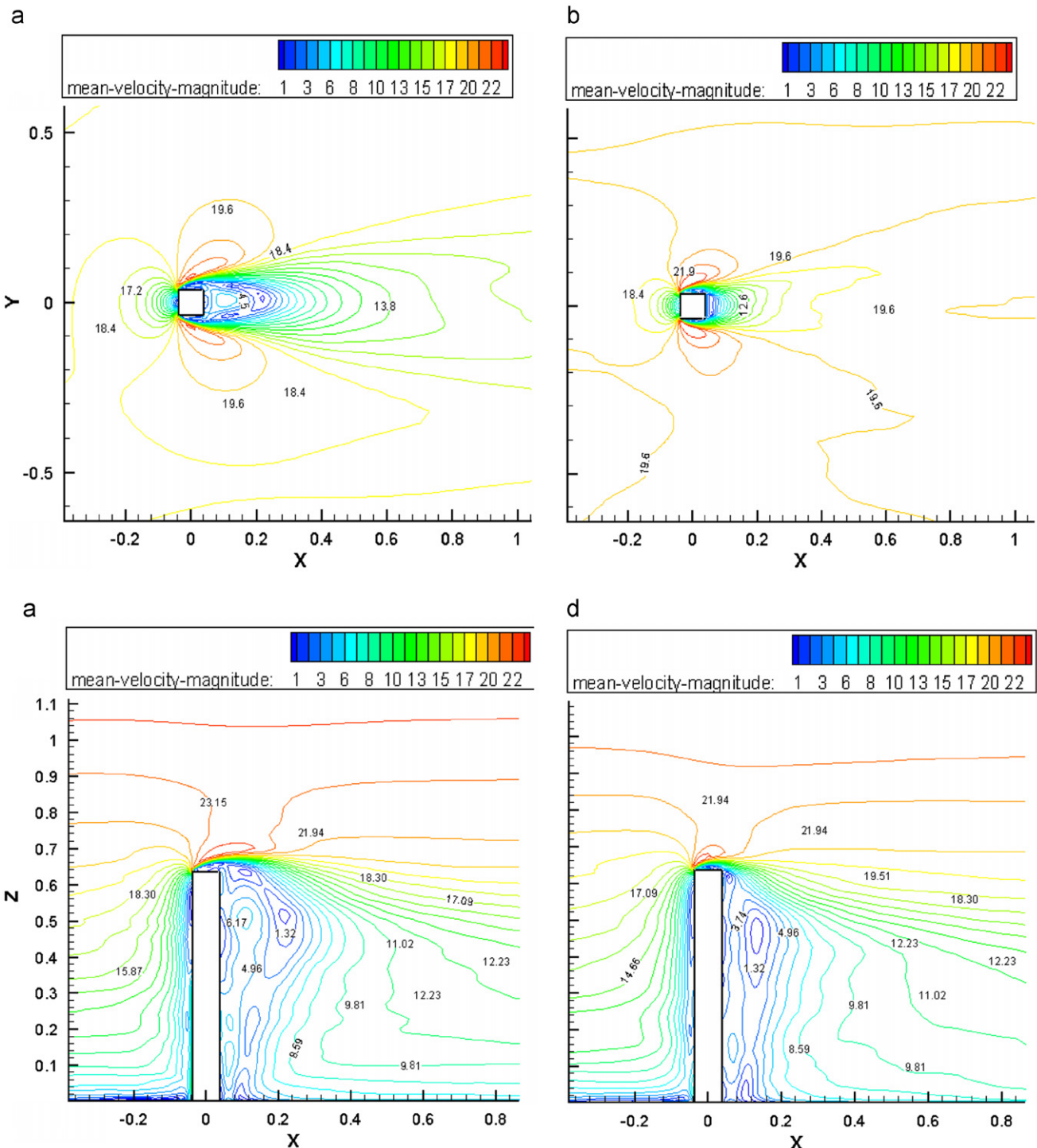


Fig. 20. Comparison of mean velocity magnitude contour predicted by the RFG and DSRFG methods. (a) By the RFG on x-y plane ($Z=0.8H$), (b) By the DSRFG on x-y plane ($Z=0.8H$), (c) By the RFG on x-z plane ($Y=0$) and (d) By the DSRFG on x-z plane ($Y=0$).

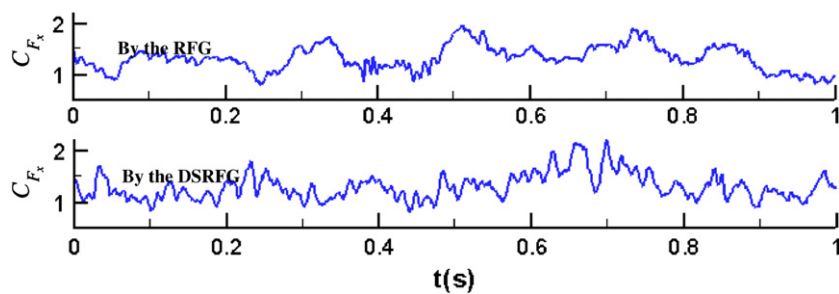


Fig. 21. Comparison of C_{F_x} time history predicted by the RFG and DSRFG methods ($Z=0.8H$).

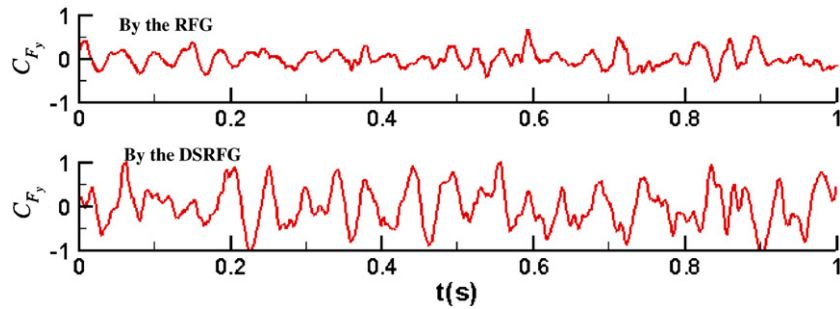


Fig. 22. Comparison of C_{F_y} time history predicted by the RFG and DSRFG methods ($Z=0.8H$).

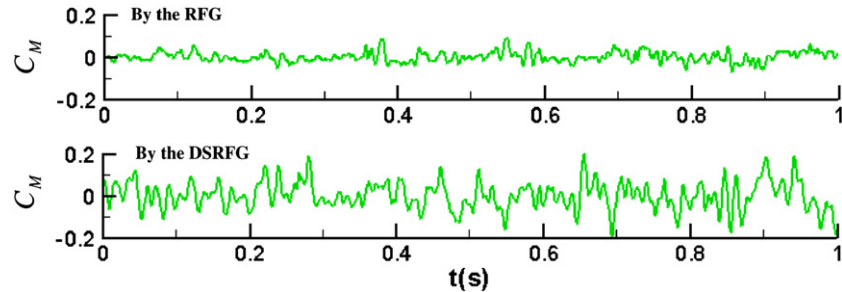


Fig. 23. Comparison of C_M time history predicted by the RFG and DSRFG methods ($Z=0.8H$).

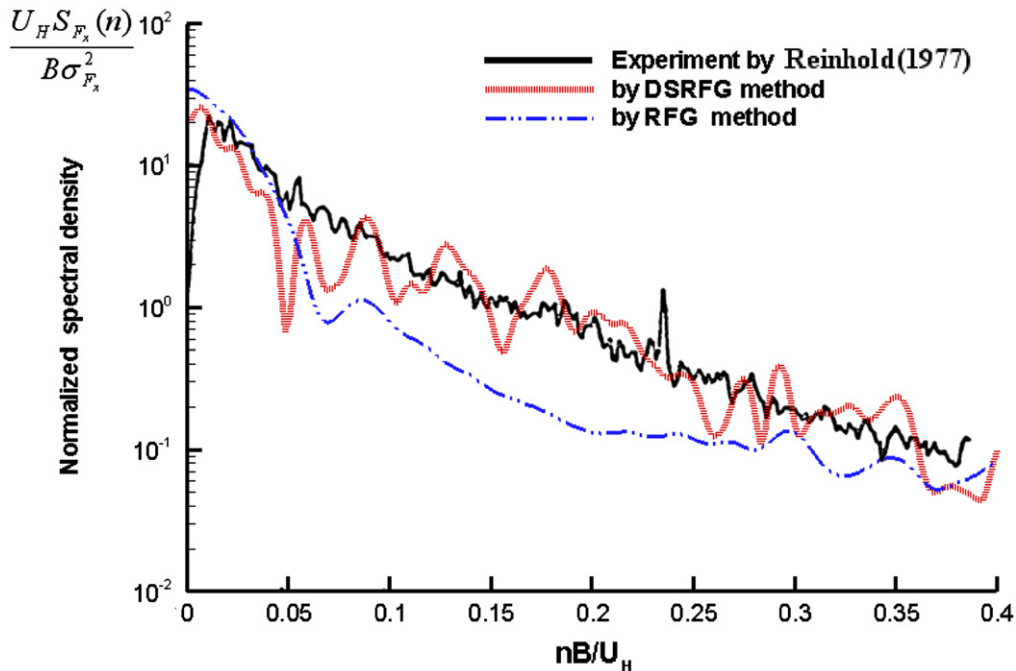


Fig. 24. Comparison of along-wind force spectra at $Z=0.8H$.

overcome the deficiency of large computational cost when increasing the sampling number of wave number and the sampling frequency of spectra.

The DSRFG method was programmed and implemented as an UDF library of FLUENT software to provide the inflow turbulence generation. The results of a wind tunnel test of a prismatic building model in simulated atmospheric boundary layer were used to verify the accuracy of the numerical results by LES with

both the RFG and DSRFG methods for generation of inflow boundary conditions. Through comparison of the numerical results by the two methods with the experimental results, it was concluded that:

- (1) Inflow turbulence generated by the DSRFG method was proved to be able to enhance the accuracy of the turbulent flow simulation and wind-induced forces on the building model due to the following improvements: (a) more realistic

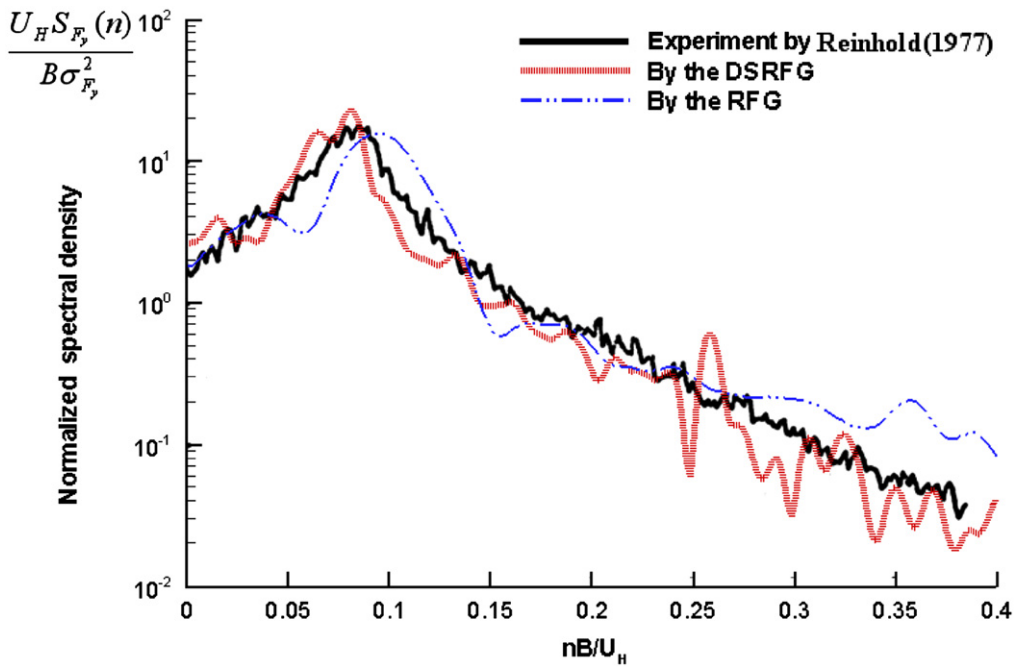


Fig. 25. Comparison of across-wind force spectra at $Z=0.8H$.

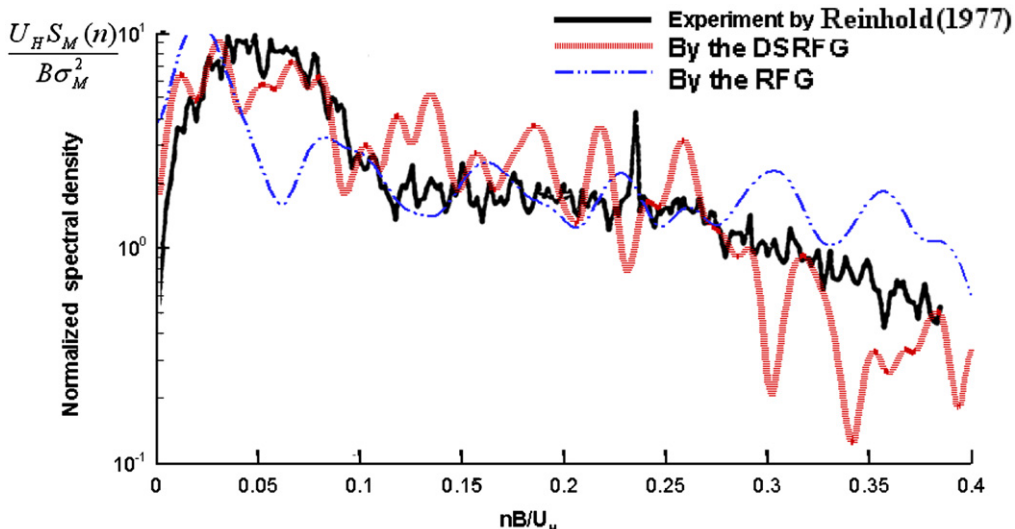


Fig. 26. Comparison of torsional moment spectra at $Z=0.8H$.

- vortices were observed in the simulated inflow turbulent flow field, which was confirmed to be useful for correctly predicting the turbulent flow development in downstream. (b) the wind-induced forces and torsional moments on the building model including rms values and spectra can be well predicted by the DSRFG, especially the along-wind forces and torsional moments, since the inertial subrange of a inflow turbulence spectrum was properly simulated by this method.
- (2) Less spatial correlation and lack of simulation of inertial subrange of spectral density in the inflow turbulence generated by the RFG method resulted in decrease of inflow turbulence intensity. Under-prediction of wind-induced forces and torsional moments as well as relatively poor agreement of their spectra with the experimental results were observed for the numerical results generated by the RFG method.

It should be acknowledged that although improvement of inflow turbulence generations can enhance the accuracy of LES results, other aspects such as the limitations of SGS models in LES as well as wall function treatments may bring computational errors. So, further efforts are needed in all aspects to improve the accuracy of LES in CWE applications.

Acknowledgements

The work described in this paper was fully supported by a grant from the Research Grants Council of Hong Kong Special Administrative Region, China (Project No: CityU 117709), a grant from City University of Hong Kong (Project No. 7002466) and a key grant from National Natural Science Foundation of China

(Project No. 90815030). The authors would like to thank Dr. Zuojin Zhu of the University of Science and Technology of China for helpful discussions. Finally, the authors are thankful to the reviewers for their useful comments and suggestions.

References

- Aubry, N., Guyonnet, R., Lima, R., 1991. Spatiotemporal analysis of complex signals: theory and applications. *Journal Statistical Physics* 64, 683–739.
- Batten, P., Goldberg, U., Chakravarthy, S., 2004. Interfacing statistical turbulence closures with large-eddy simulation. *AIAA Journal* 42, 485–492.
- Bechara, W., Bailey, C., Lafon, P., 1994. Stochastic approach to noise modeling for free turbulent flows. *AIAA Journal* 32 (3), 455–463.
- Fluent, Inc, 2003. The user guide of Fluent 6.2.
- Fung, J., Hunt, J., Malik, N., Perkins, R., 1992. Kinematic simulation of homogeneous turbulence by unsteady random Fourier modes. *Journal Fluid Mechanics* 236, 281–318.
- Hemon, P., Santi, F., 2007. Simulation of a spatially correlated turbulent velocity field using biorthogonal decomposition. *Journal of Wind Engineering and Industrial Aerodynamics* 95 (1), 21–29.
- Hinze, J.O., 1975. Turbulence. McGraw-Hill, New York.
- Hoshiya, M., 1972. Simulation of multi-correlated random processes and application to structural vibration problems. *Proceedings of JSCE* 204, 121–128.
- Issa, R.I., 1986. Solution of implicitly discretized fluid flow equations by operator splitting. *Journal of Computational Physics* 62, 40–65.
- Iwatani, Y., 1982. Simulation of multidimensional wind fluctuations having any arbitrary power spectra and cross spectra. *Journal of Wind Engineering* 11, 5–18.
- Jarrin, N., Benhamadouche, S., Laurence, D., Prosser, R., 2006. A synthetic-eddy method for generating inflow conditions for large-eddy simulations. *International Journal of Heat and Fluid Flow* 27 (4), 585–593.
- Keating, A., Piomelli, U., Balaras, E., Kaltenbach, H.J., 2004. A priori and a posteriori tests of inflow conditions for large-eddy simulation. *Physics of Fluids* 16, 4696.
- Klein, M.A., Sadiki, Janicki, J., 2003. A digital filter based generation of inflow data for spatially developing direct numerical or large eddy simulations. *Journal of Computational Physics* 186, 652–665.
- Kondo, K., Murakami, S., Mochida, A., 1997. Generation of velocity fluctuations for inflow boundary condition of LES. *Journal of Wind Engineering and Industrial Aerodynamics* 67&68, 51–64.
- Kraichnan, R.H., 1970. Diffusion by a random velocity field. *Physics of Fluids* 13 (1), 22–31.
- Li, A., Ahmadi, G., Bayer, R., Gaynes, M., 1994. Aerosol particle deposition in an obstructed turbulent duct flow. *Journal of Aerosol Science* 25 (1), 91–112.
- Li, Q.S., 1996. The effects of turbulence on streamwise surface pressures in separated and reattaching flows, Ph.D. Thesis, Monash University, Australia.
- Li, Q.S., Xiao, Y.Q., Wong, C.K., Jeary, A.P., 2004. Field measurements of typhoon effects on a super tall building. *Engineering Structures* 26, 233–244.
- Li, Q.S., Xiao, Y.Q., Wong, C.K., 2005. Full-scale monitoring of typhoon effects on super tall buildings. *Journal of Fluids and Structures* 20, 697–717.
- Li, Q.S., Xiao, Y.Q., Fu, J.Y., Li, Z.N., 2007. Full scale measurements of wind effects on the Jin Mao Building. *Journal of Wind Engineering and Industrial Aerodynamics* 95, 445–466.
- Lilly, D.K., 1992. A proposed modification of the germano subgrid-scale closure model. *Physics of Fluids* 4, 633–635.
- Liu, K.L., Pletcher, R.H., 2006. Inflow conditions for the large eddy simulation of turbulent boundary layers: a dynamic recycling procedure. *Journal of Computational Physics* 219 (1), 1–6.
- Lumley, J.L., Panofsky, H.A., 1964. The Structure of Atmospheric Turbulence. Wiley-Interscience, New York, pp. 239.
- Maruyama, T., Morikawa, H., 1994. Numerical simulation of wind fluctuation conditioned by experimental data in turbulent boundary layer. In: Proceeding of the 13th Symposium on Wind Engineering, pp. 573–578.
- Mathey, F., Cokljat, D., Bertoglio, J.P., Sergent, E., 2006. Assessment of the vortex method for large eddy simulation inlet conditions. *Progress in Computational Fluid Dynamics* 6, 1–3.
- Reinhold, T.A., 1977. Measurement of simultaneous fluctuating loads at multiple levels on a tall building in a simulated urban boundary layer, Ph.D. Thesis, Virginia Polytechnic Institute & State University, U.S.A.
- Schluter, J.U., Pitsch, H., Moin, P., 2004. Large eddy simulation inflow conditions for coupling with Reynolds-averaged flow solvers. *AIAA Journal* 42 (3), 478–484.
- Shirani, E., Ferziger, J.H., Reynolds, W.C., 1981. Mixing of a passive scalar in isotropic and sheared homogeneous turbulence, Report TF-15, Mech. Eng. Dept., Stanford Univ.
- Simiu, E., Scanlan, R.H., 1996. Wind Effects on Structures—Fundamentals and Applications to Design. John Wiley & Sons, Inc., New York.
- Smirnov, R., Shi, S., Celik, I., 2001. Random flow generation technique for large eddy simulations and particle-dynamics modeling. *Journal of Fluids Engineering* 123, 359–371.
- Tamura, T., 2000. Towards practical use of LES in wind engineering. *Journal of Wind Engineering and Industrial Aerodynamics* 96 (10–11), 1451–1471.
- Yoshihide, T., Akashi, M., Ryuichiro, Y., Hiroto, K., Tsuyoshi, N., Masaru, Y., Taichi, S., 2008. All guidelines for practical applications of CFD to pedestrian wind environment around buildings. *Journal of Wind Engineering and Industrial Aerodynamics* 96, 1749–1761.